

Drew University
College of the Liberal Arts

Heterogeneous Uptake of O₃ and SO₂ on Kaolinite as a Function of Atmospheric Processing

A Thesis in Chemistry

By

Zoe Coates Fuentes

Submitted in Partial Fulfillment
Of the Requirements
For the Degree of
Bachelor in Arts
With Specialized Honors in Chemistry

May 2018

Acknowledgments

I would first like to thank my research advisor, Dr. Ryan Hinrichs. Without his constant support, feedback, and encouragement I would not have been able to complete this particular hurdle in my undergraduate career. Throughout the last four years he has provided me with the best mentorship and opportunities I could have asked for, showing me that the first step in the academic pursuit of knowledge is finding enjoyment in the work that you do. I would also like to thank my second reader, Dr. Mary-Ann Pearsall, whose thorough feedback constantly pushed me to question the very fabric of my arguments and whose encouragement and appreciation have pushed me to become a better student and scientist. To my third reader, Dr. Timothy Carter, I owe thanks for immersing himself in an area outside of his usual expertise and providing incredibly insightful feedback, along with an outside perspective which helped me ground the science of my argument in the context of climate change politics. I would like to thank past Hinrichs lab students, particularly Madeline Lederer, Theresa Kuckinski, Dani Levis, and Jed-Joan Edziah for laying the foundations for the research that I developed.

I would also like to thank my friends and family for their constant support throughout this writing process, and particularly Kevin DePope, who made sure to provide constant comedic relief throughout our time in the lab.

I would finally like to thank the Drew University Chemistry Department, the National Science Foundation, the Baldwin Honors Program, and the Drew Summer Science Institute for providing the funding and opportunities that made my undergraduate research experience possible.

Table of Contents

Acknowledgments	2
Abstract	4
Chapter 1: Introduction	5
1.1 Jing-Jin-Ji: A Case Study of Pollution and its Impact on Atmospheric Aerosol	5
1.2 Atmospheric Reactivity of O ₃ , SO ₂ , and Mineral Dust	14
1.3 Our Research: Increasing the Complexity of Laboratory Measurements	27
Chapter 2: Experimental Methods	30
2.1 Flow Tube Parameters and Characterization	32
2.2 Experimental Procedure	36
2.2.1 O ₃ Analysis	36
2.2.2 VOC Processing of Kaolinite	44
2.2.3 SO ₂ Synthesis	45
2.2.4 SO ₂ Analysis	46
Chapter 3: Results and Discussion	51
3.1 Reactivity of O ₃ on Pure Kaolinite	51
3.2 Determination of the Relative Humidity Dependence of O ₃ Uptake	55
3.3 Impact of Surface Adsorbed Volatile Organic Compounds (VOC's)	62
3.4 Effect of O ₃ Concentration on Rate of Uptake	71
3.5 Impact of SO ₂ on O ₃ Reactivity	74
Chapter 4: Conclusion	80
4.1 Summary of Main Results	80
4.2 Areas for Future Work	82
Work Cited	86

Abstract

Mineral dust aerosol, suspended particulates that exist within the atmosphere due primarily to dust storms in arid regions, serve as reactive surfaces for other atmospheric species, including O₃, SO₂, and volatile organic compounds (VOCs). Studying the reactivity of these mineral surfaces under atmospherically relevant conditions is instrumental in developing a comprehensive understanding of the destruction of tropospheric O₃, which is closely related to high levels of pollution. For this study, a laminar flow reactor, coupled with an ozone detector, was used to monitor the O₃ uptake on kaolinite, an aluminosilicate clay, as a function of relative humidity, VOC pre-coating, and simultaneous SO₂ reactivity. Steady state reactive uptake coefficient ($\gamma_{\text{BET},\text{O}_3}$) calculations quantified the number of reactive collisions between ozone molecules and the mineral surface at average dose points of 4,000-10,000 ppb-min. Data show a 75.8-90.2% decrease in $\gamma_{\text{BET},\text{O}_3}$ at higher relative humidity (RH) consistent with competitive adsorption of water onto the surface. When holding RH constant at 25%, O₃ uptake increased by two orders of magnitude for dusts that have been pre-exposed to limonene and α -pinene, showing an introduction of further reactive sites due to the adsorbed products of these VOCs with the surface. Furthermore, exposure to SO₂ also showed increased uptake of O₃ by two orders of magnitude, indicating possible sulfate formation on the kaolinite surface. Reactivity with α -pinene -processed kaolinite showed that the VOC dominated uptake reactivity, though sustained uptake of SO₂ indicated the possible formation of organosulfates. The introduction of greater complexity into the laboratory experiments of O₃ on kaolinite provides more accurate representations of atmospheric chemistry to be used for computational models and eventual policy recommendations. We recommend uptake values of 10^{-7} for VOC and SO₂ processed kaolinite.

Chapter 1: Introduction

As air quality and public health become key issues at the forefront of many countries' public policy agendas, greater attention is being given to issues of pollution and atmospheric emissions. Among the countries who have shown the greatest initiative is China, given its large dependence on coal burning as a source of heating and electricity. In recent years, Chinese air quality has become the object of widespread concern, as millions die from exposure to particulates associated with respiratory cardiovascular disease, myocardial infarctions, and lung cancer, among others. In light of the severe implications that air quality can have over a population's livelihood and health, explaining trends in emissions and alternatives for major pollutants may lead to policy recommendations for high-incidence countries such as China. In order to develop an understanding of these complex atmospheric conditions, policymakers and scientists alike turn to computational models to determine the key players in air quality and their overall contributions to global atmospheric processes. This chapter will outline major concerns in global and regional air quality, will provide a context for the influence of computational models on a government's ability to develop environmental policy and will explain the dependence of these complex computational models on laboratory measurements.

1.1 Jing-Jin-Ji: A Case Study of Pollution and its Impact on Atmospheric Aerosol

In recent years, China has received increasing attention from the international community due to its rapidly declining air quality. According to the Chinese Ministry of Health, 265 of the 338 major Chinese cities exceeded the national air quality health standards in 2016 (Jia and Wang 2017). Given this widespread distress on air quality, the

Beijing-Tianjin-Hebei region, China's most highly urbanized region, Jing-Jin-Ji for short, has become the center of multiple research studies monitoring air quality variation and its relation to atmospheric aerosol species.

Present research indicates that particulate matter, PM_{10} and $PM_{2.5}$, is strongly correlated with cardiovascular and respiratory health disorders, and thus PM_{10} concentrations, have often been used as a reference for air quality. The most widely accepted classification for particulate matter places particles in two categories: fine particles, with less than $2.5 \mu\text{m}$ in diameter ($PM_{2.5}$), and coarse particles, with diameters between 2.5 and $10 \mu\text{m}$ (PM_{10}). The former originates primarily from combustion sources, while the latter encompasses material released through mechanical processes such as "construction activities, road dust re-suspension, and wind", and mineral dust storms (WHO 2005).

For Jing-Jin-Ji's case in particular, the main culprit in exposing its population to hazardous chemicals is the formation of a thick haze, composed primarily of $PM_{2.5}$ which has been aerosolized and remains suspended in the atmosphere as a thick smog. In 2017, two large episodes of high $PM_{2.5}$ were recorded in Jing-Jin-Ji with concentrations surpassing $500 \mu\text{g}/\text{cm}^3$ (Jia and Wang, 2017), which is not only 14 times higher as the US EPA's standard (EPA 2016) but also 20 times higher than WHO's $25 \mu\text{g}/\text{cm}^3$ 24-hour mean guideline (WHO 2005). In perspective, US cities around the same time recorded a maximum around $50 \mu\text{g}/\text{cm}^3$. Research into the presence of airborne pollutants in downtown Beijing has identified gasoline, coal, and diesel combustion as the largest contributors to particle-bound hydrocarbon pollution, with coal-burning representing a

significant driver for heightened winter concentrations (Shen et al., 2018). Particle-bound hydrocarbons are of additional concern given their demonstrated influence over premature deaths due to lung cancer, with risk levels above WHO's accepted standard (Yin and Xu, 2018).

In addition to their implications for public health in the region, these aerosolized $PM_{2.5}$ and PM_{10} species also affect atmospheric regulation and balance. Since these species are essentially suspended particulates that remain in the atmosphere due to their light mass, they are able to interact with other species in the atmosphere, among them other pollutants, solar radiation, and greenhouse gases such as water. Depending on their size and chemistry, aerosols are able to remain in the atmosphere for longer periods of time, up to more than two weeks in the case of smaller particles, or shorter periods of time for larger particles; the longer a particulate's lifetime in the atmosphere, the more likely it is to react and contribute to atmospheric conditions (Buseck and Posfai, 1999).

Despite claims that China's pollution problem is solely based on poor industrial processes that emit harmful particulates, numerous factors affect current ambient air quality in the region. For instance, Jing-Jin-Ji, is located in a valley, which leads to increased air stagnation, as the surrounding mountains don't allow for air diffusion (Jia and Wang, 2017). Moreover, smog constituents have shown dramatic seasonal variations in the Beijing region. During summer and autumn months, higher concentrations of "biomass burning derived particles" are observed, whereas winter months show increased coal combustion, and spring months show exacerbated mineral dust presence. For all seasons, however, the largest chemical species mass percent contributors were SO_4^{2-} , NO_3^- , and

NH_4^+ , though their exact pathways of formation remain unknown (Shen et al., 2018). For Jing-Jin-Ji in particular, atmospheric sulfate (SO_4^{2-}), present in the form of sulfuric acid and sulfate salts, appears to be the largest contributor to poor air quality.

Given the large role SO_4^{2-} plays in air quality in the region, understanding its main sources allows for the development of better regulation strategies by the appropriate authorities. Various studies have associated SO_4^{2-} production, particularly in areas of high fossil fuel combustion and pollution, with the oxidation of SO_2 by NO_2 and O_3 , all three themselves classified as criteria air pollutants by the EPA (2015). As coal combustion in particular increases, sulfur dioxide and nitrogen oxides are released, a process that allows them to interact with other atmospheric species, resulting in the formation of haze and secondary aerosol (Jia and Wang, 2017). More importantly, SO_2 can be oxidized to form SO_4^{2-} particulates, highly reflective surfaces associated with pollution and a main component of Jing-Jin-Ji's haze episodes. Though the exact pathway of atmospheric SO_2 oxidation is uncertain, researchers propose the aqueous oxidation in aerosolized water under high relative humidity (Finlayson-Pitts and Pitts, 2000). In fact, other researchers have contended that adsorbed water on mineral aerosol could also serve as a sufficient aqueous interface for SO_2 oxidation (Yu et al., 2017). As a known precursor to SO_4^{2-} , isolated SO_2 reactivity could provide insight into available pathways for oxidation and as such could inform the Chinese government on prospective regulatory policies.

In order to develop comprehensive regulatory policies, it is necessary to have a broad understanding of the interplay of variables that affect the chemistry of a region. In Jing-Jin-Ji's case, proximity to arid regions, mainly the Gobi Desert, brings with it an influx

of mineral aerosol which can serve as a reactive surface for other species. Furthermore, as these dusts remain in the atmosphere for weeks at a time, they can undergo processing by different natural and anthropogenic compounds, among them volatile organic compounds (VOCs) emitted from vegetation.

In light of the catastrophic implications that current air quality has on regional public health, particularly for those living in Jing-Jin-Ji, there is an urgent need for development of regulatory policies that target the most harmful pollutants with associated health risks. Unfortunately, current understanding of these processes and pollutants is limited and the evaluation of atmospheric conditions quickly becomes muddled with the plethora of intervening variables. Consequently, in order to properly develop an understanding of declining air quality not only in China but worldwide, governments and research institutions have started using computational models to simulate air quality variations. These models rely on experimental parameters developed in isolated laboratory systems with controlled conditions. As such, the models themselves can be restrictive, as they are based on experiments run under conditions not considered atmospherically relevant. For this reason, if models are to be used for policy development, accurate parameters are needed in order to develop realistic expectations for emissions and pollution control.

In order to conceptualize these complex systems, we select laboratory variables that help replicate real-world factors such as pollution, land-use, and atmospheric conditions, as seen in Figure 1. In the case of pollution, we measure the presence of criteria air pollutants such as SO₂ and O₃, key factors in the current global understanding of air quality.

Land use factors influence the emission of mineral particles and VOCs into the atmosphere and so current laboratory experiments also account for the presence of particulates from arid regions, such as mineral dust, serving a role in chemical systems. Though SO_2 , O_3 , and mineral dust have been studied in prior laboratory work (Li et al., 2007) for atmospheric chemistry models, atmospheric chemistry possesses much greater complexity than has been studied. For instance, the vast body of scientific literature largely neglects the influence of relative humidity and VOCs, both of which can adsorb to the mineral particle.

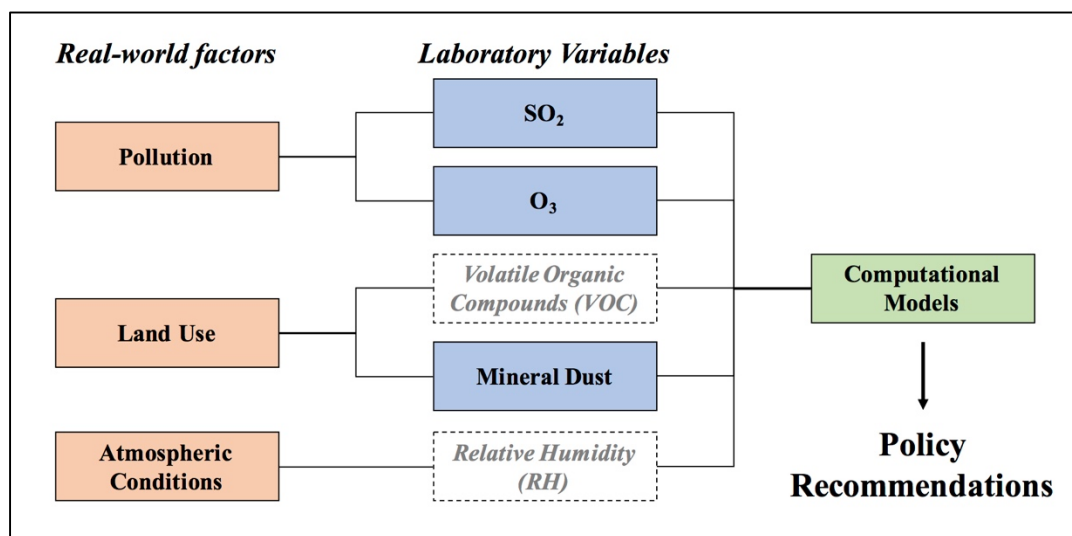


Figure 1. Schematic representation of the experimental development process to replicate real-world factors by employing laboratory variables that can be measured to provide parameters for computational modeling systems. Scheme shows the selection of specific laboratory experiments that will model pollution, land use, and atmospheric conditions, with the end goal of obtaining more accurate parameters for atmospheric computational models. However, current studies neglect variables such as volatile organic coatings and relative humidity (shown in grey), which are key properties and processes within the atmosphere.

Our experimental system seeks to address the broader complexities of atmospheric chemistry, accounting for variables such as relative humidity and the fact that mineral

particles often have adsorbed organic compounds, in order to ensure that the numbers are not only accurate but also relevant to the broader atmospheric context. Figure 2 shows the incorporation of additional experimental variables to fortify the parameters provided for computational models.

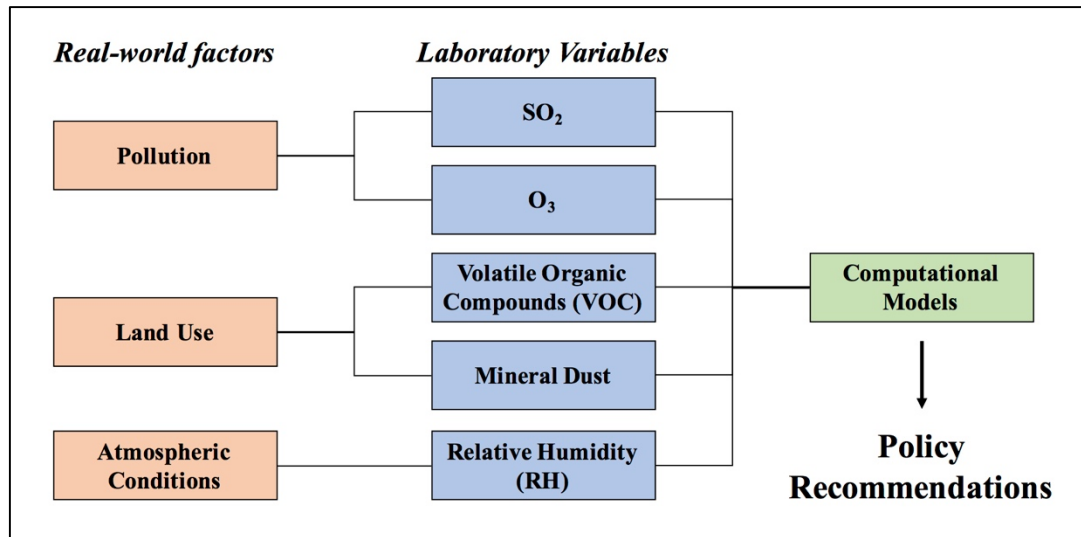


Figure 2. Schematic representation of the improvement of experimental design to replicate real-world atmospheric conditions through the incorporation of greater complexity in land use and atmospheric conditions. Scheme shows the incorporation of VOC coating and relative humidity as key variables for the characterization of atmospheric systems.

Among the examples of current computational models is Wang et al.'s implementation of the United States Environmental Protection Agency's Multiscale Air Quality modeling system to predict ozone concentrations (2012). For their study, they took into account multiple variables and found that modeling studies vary significantly depending on their consideration of dust emission and transport, climatology, and the nature of the dust itself. Furthermore, they posited that interactions with other species could affect the total uptake of species such as O₃. As a consequence, if a computational model

is based on experimental results run under isolated O₃ conditions, it will provide tenuous predictions of O₃ variability, hence creating a precarious foundation for policymakers seeking scientific expertise.

While research labs are becoming increasingly more aware of the complexity of atmospheric chemistry, concentration projections and computational models still remain limited in their consideration of variable factors. In fact, studies into the reactivity of various atmospheric species such as mineral dust don't take into consideration sources of processing for the dust such as exposure to VOCs or criteria air pollutants during transport, thereby providing a limited view of aerosol chemistry beyond their source regions.

In essence, to understand the complexity of regional air quality in Jing-Jin-Ji, it is necessary to first characterize the reactivity of each of the constituent components that may come into play during haze episodes. Moreover, to determine the variables that are present within PM_{2.5} and PM₁₀ chemistry, it is essential to pinpoint where these interactions take place. At their most general, these interactions usually occur in the lower level of the atmosphere, the closest to Earth's crust, as seen in Figure 3.

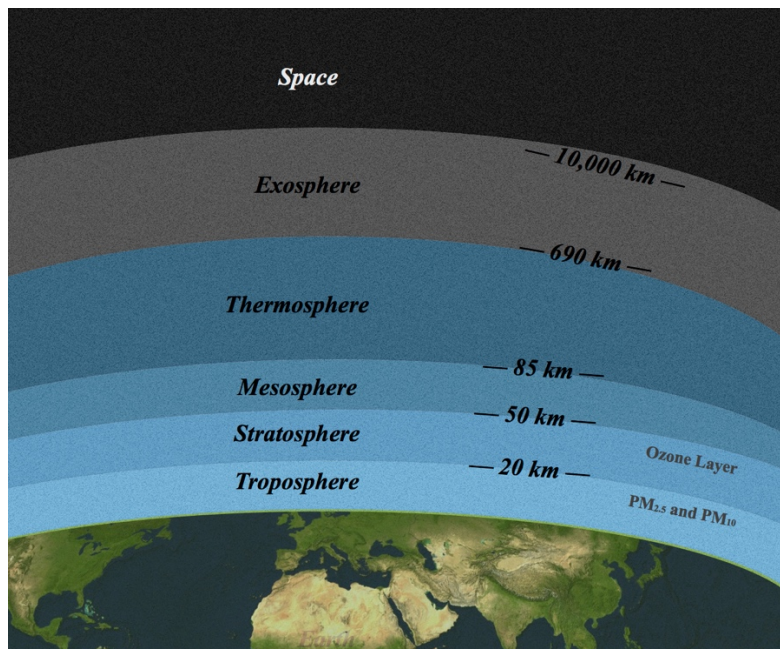


Figure 3. Representation of the five layers of the atmosphere by their distance from Earth's surface. For studies analyzing PM_{2.5} and PM₁₀, the main layer of focus is the troposphere, the lowest layer of the atmosphere.

During their time in the troposphere, PM_{2.5} and particularly PM₁₀ are transported from their source regions to other destinations. From these transport processes, further chemistry can be observed, as aerosol travel over forested terrain, industrialized and urbanized regions, and humid environments, among others. Furthermore, mineral dust may provide a surface for heterogeneous reactivity of gaseous O₃ and SO₂, which are main precursors for SO₄²⁻ in the atmosphere. In the following sections, I will provide context for four main components of atmospheric reactivity: tropospheric O₃ and SO₂, mineral dust, and atmospheric processing by VOCs.

1.2 Atmospheric Reactivity of O₃, SO₂, and Mineral Dust

Atmospheric O₃ has been a highly debated species within international climate change policy mainly due to its connection to ultraviolet radiation protection. The O₃ layer, as the main point of attention for policy-makers and activists worldwide, consists of a layer of O₃ gas located in the stratosphere, or the second lowest layer of the atmosphere. In fact, approximately 90% of atmospheric O₃ is located within the stratosphere, serving as a protective layer that absorbs ultraviolet radiation and thus limits its ability to reach Earth's surface. However, the remaining 10% of atmospheric O₃, which resides in the troposphere, plays a less benign role in atmospheric gas regulation, as it guides the formation of the hydroxyl radical, a key player in atmospheric oxidative processes, seen in reactions 1 and 2 (Levy, 1971).



Tropospheric O₃ has been classified by the EPA as a criteria air pollutant due to its possible harmful effects to human health, particularly through respiratory disorders. In the lower atmosphere, O₃ most commonly originates from precursors emitted by industrial facilities, electric utilities, and motor vehicles, as well as forming from reactions between natural chemicals from plants (EPA, 2015). In light of this, understanding how different processes can affect atmospheric concentrations of O₃ allows for a better prediction of future events and how they can influence human and ecosystem survival.

In their influential atmospheric global-transport chemistry model, Lelieveld and Dentener researched the applicability of existing theories of tropospheric O₃ sources: *in*

situ photochemistry and O₃ exchange from the stratosphere (2000). The former, involves photo-dissociation of pre-existing trace gases, primarily nitrogen dioxide (NO₂), present in the atmosphere due to emissions through energy use, industrial processes, biomass burning, agriculture, natural vegetation and soils, lightning, and NO_y from the stratosphere. The latter, however, relies on meteorological processes and their influence on interlayer transport. For their study, Lelieveld and Dentener found that *in situ* photochemistry is the main source of tropospheric O₃, though stratosphere-troposphere exchange still exerts a role in tropospheric concentrations (Lelieveld and Dentener, 2000). The main pathways for atmospheric production of O₃ can be seen in Figure 4.

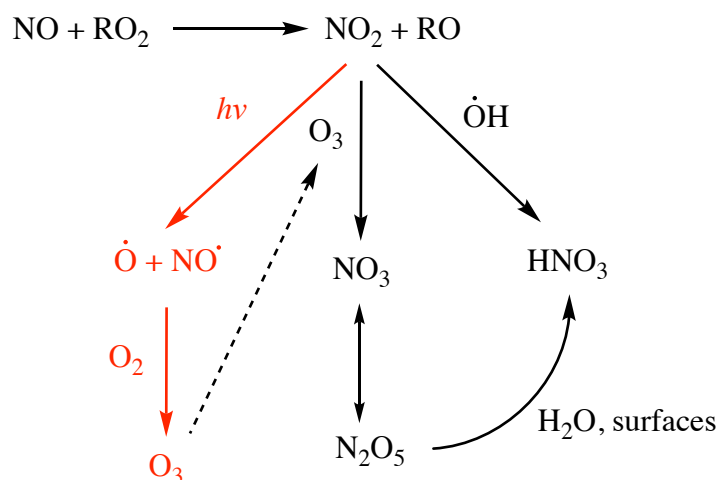


Figure 4. Main reaction paths for NO_x in air, including the formation of O₃. The figure shows the formation of NO₂ from alkyl peroxy (RO₂) and NO. The resulting NO₂ can then react through photolysis or oxidation by O₃ and OH to yield NO, NO₃, or nitric acid HNO₃). The figure highlights the primary known pathway for O₃ formation through the photolysis of NO₂ to form reactive NO and O radicals which can react with O₂ (red). (Finlayson-Pitts and Pitts, 1997)

The main reaction path for O₃ formation involves the photo-reduction of NO₂ from outdoor air pollution. The highest global concentrations of NO₂ can be seen in

northeastern China, particularly in the region of Jing-Jin-Ji, as can be seen in Figure 5 with data from NASA's Ozone Monitoring Instrument, which measures global NO₂ concentrations. As such, it provides a prediction of possible O₃ concentrations, based on the availability of its NO₂ precursor.

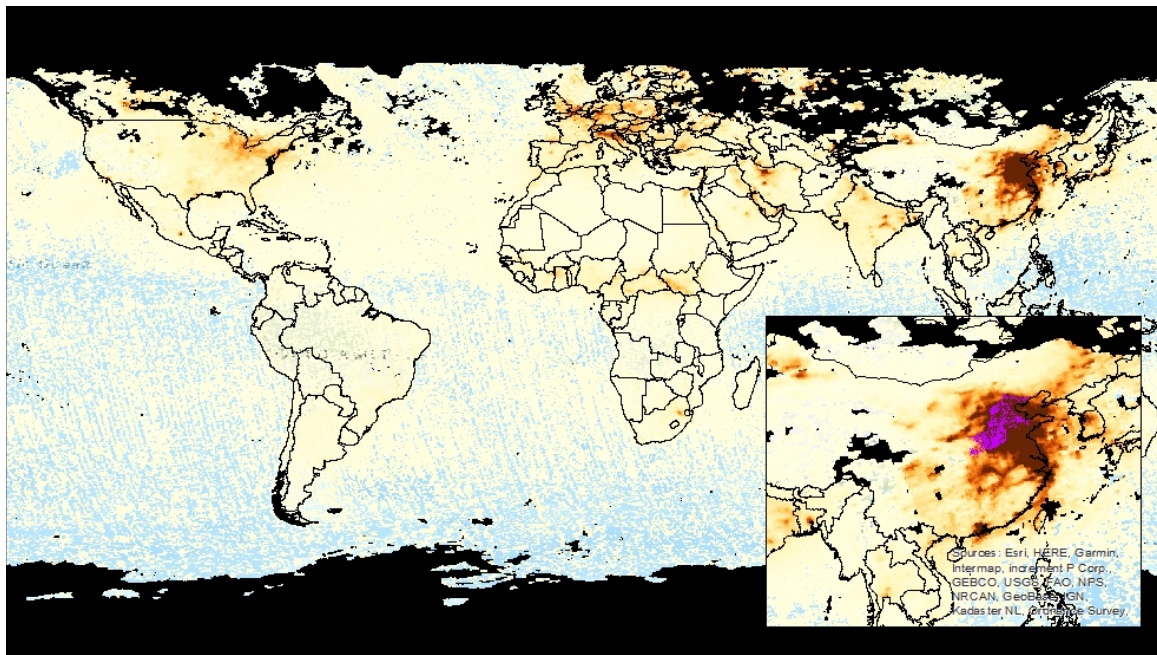


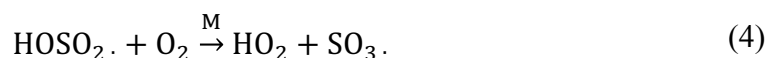
Figure 5. Global NO₂ concentrations, as measured by the Ozone Monitoring Instrument on NASA's Aura Satellite, in Asia during December, 2017. Image shows heightened NO₂ concentrations in northeastern China, as accentuated by the enlarged image (lower right). The image particularly highlights the importance of studying the Beijing Tianjin urban region (pink), given its location in the highest density area for NO₂ (NASA Neo and Natural Earth for cultural divisions and Jing-Jin-Ji urban area).

As a strong atmospheric oxidant and criteria air pollutant itself, O₃ presents a possible route for atmospheric SO₂ oxidation. Given NO₂'s high availability in regions such as Jing-Jin-Ji, increased O₃ emissions could help explain trends in SO₄²⁻ formation.

This in turn could help elucidate possible areas of regulation for environmental emission policy.

Tropospheric SO₂ most commonly originates from the combustion of fossil fuels containing sulfur, such as coal (Finlayson-Pitts and Pitts, 2000). Upon emission, the SO₂ is oxidized to form sulfates and sulfuric acid. However, the exact process of SO₂ oxidation is unknown. Research studies have thus far investigated the gas-phase and aqueous-phase oxidation of SO₂; our research seeks to analyze mineral dust surfaces as an alternate pathway for SO₂ oxidation.

Initial studies into SO₂ oxidation in the atmosphere sought to determine the main loss pathways available to this species. To begin analyzing the behavior of SO₂, they employed gas-phase reactivity analyses. The main pathway for SO₂ gas-phase oxidation involves the hydroxyl radical (Finlayson-Pitts and Pitts, 2000). Through reactions 3 and 4, you see the formation of a free radical which then reacts with diatomic oxygen to form hydroperoxyl and another radical adduct.



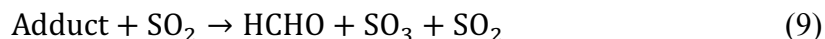
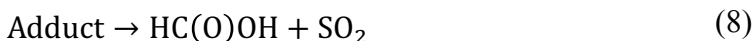
The hydroperoxyl radical can also further react under the presence of NO to regenerate the OH radical, following reaction 5, which can continue to oxidize atmospheric species.



Following reaction 6, however, SO₃· reacts readily with water to form gaseous sulfuric acid, considered the main product of gas-phase SO₂ oxidation and a main component of acid rain.



An alternate pathway that has been considered is the oxidation of SO_2 by the Criegee biradical ($\text{HC}^{\cdot}\text{HOO}^{\cdot}$), particularly in instances where photochemistry is reduced so concentrations of OH are limited (Finlayson-Pitts and Pitts, 2000). Criegee reactivity entails the oxidation formation of the criegee biradical by O_3 under the presence of an alkene. These reactive intermediate can react with SO_2 to form a reactive adduct, through reaction 7, which can react with another SO_2 to form additional products, through reactions 8 and 9.



For these processes, however, water was found to be inhibitory, which was attributed to the fact that there was competitive reactivity between the SO_2 and water with the Criegee intermediate (Finlayson-Pitts and Pitts, 2000).

All of these pathways presented are gas-phase reactions, however, they cannot account for the rates of SO_4^{2-} formation observed in the atmosphere. Though gas-phase reactivity answers part of the question, atmospheric conditions allow for more complex reactivity than that described by gas-phase experiments. For instance, the presence of suspended water droplets in aerosol, fog, clouds, and even rain could provide additional interfaces for SO_2 reactivity. For this reason, researchers started looking into the aqueous-phase reactivity of SO_2 as a possible pathway for SO_2 oxidation.

SO₂ gas dissolves readily in water in a manner similar to CO₂, forming three main species: hydrated SO₂ (SO₂•H₂O), the bisulfite ion (HSO₃⁻), and sulfite (SO₃²⁻), which exist in equilibrium with each other. These species all possess the same +4 oxidation state for the sulfur, representing its less oxidized form. Once in solution, the S(IV) species can be oxidized by dissolved oxidants such as O₂, O₃, H₂O₂, free radicals such as OH and HO₂, and nitrogen oxides (NO_x) (Finlayson-Pitts and Pitts, 2000). In most cases, aqueous-phase reactivity follows the process outlined in Figure 6, where the SO₂ is transported across the air-water interface, where it attains an equilibrium and is then transported into the bulk phase, where oxidation into S(VI) occurs.

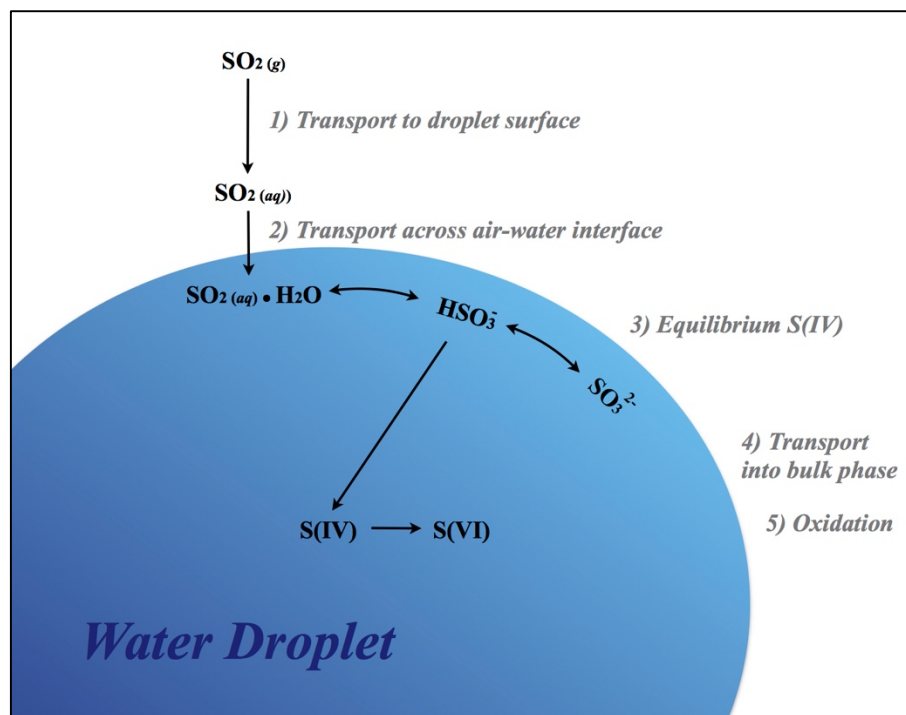


Figure 6. SO₂ aqueous-phase oxidation in an atmospheric water droplet.

Schematic shows the transport of gaseous SO₂ to the droplet surface and across the air-water interface, where it is able to establish an equilibrium between its three main dissolution S(IV) species (SO₂•H₂O, HSO₃⁻, SO₃²⁻). Upon equilibrium, it is transferred into the bulk water phase near the center of the droplet, where it can be

oxidized to the S(IV) form (Finlayson-Pitts and Pitts, 2000).

These processes provide a different interface for reactions to occur, enabling the reaction of these S(IV) species with different oxidants than those characteristic of gas-phase chemistry. However, different heterogeneous solid interfaces could also play a part in atmospheric SO₂ oxidation. In fact, adsorption of SO₂ onto aerosolized particulates like graphite and soot has been found to lead to surface-driven oxidation. In these systems, water fosters greater sulfate production through the formation of an aqueous interface on the solid surface (Finlayson-Pitts and Pitts, 2000). For China, the proximity of the Gobi desert as a source of mineral dust introduces another possible interface for solid-gas chemistry.

Mineral aerosol are suspended dust particulates in the atmosphere due primarily to dust storms in arid regions; when strong winds come in contact with dry soil, the influx of these dusts into the troposphere sees a drastic increase (Woodward et al., 2005). The amount of mineral dust loading into the atmosphere is estimated to average 1000-3000 Tg per year, greatly depending on the location and the season, with the Sahara Desert acting as the largest global contributor (IPCC, 2001). The largest mineral aerosol contributions currently come from “the west coast of North Africa and extending through the Middle East and into Central Asia”, with 90% of the dust generation currently occurring in the Northern Hemisphere (Usher et al., 2003). However, given rising desertification around the world, current prediction models of aerosol loading estimate an increase in emissions,

with new source areas expanding primarily in the Southern Hemisphere, including the Southern Pacific, South America, and Australia (Woodward et al., 2005).

Mineral aerosol abundance depends greatly on regional environmental factors such as wind velocity, soil moisture and cohesiveness, and terrain vegetation coverage. Consequently, heightened soil aridity and increased desertification of land around the world exacerbate the influx of aerosol into the atmosphere. Given that “improper agricultural and grazing practices can account for 20-50%” of the dust influx into the atmosphere, understanding the role that these particulates play can provide policymakers with further incentives to promote sustainable agricultural practices (Usher et al., 2003). At the current rate, with continued anthropogenic drivers, atmospheric mineral dust loading is expected to increase by about 10% before the year 2100 (Usher et al., 2003).

Having entered the troposphere, mineral dusts are able to have significant impacts on atmospheric chemistry, human health, climate, and biogeochemical cycles. Furthermore, as aerosol participate in environmental processes, they can exacerbate the effect of current climate change drivers and alter chemical dynamics through feedback mechanisms such as dieback of vegetation and animals, changes in radiative forcing, increased cloud condensation, variable rainfall, and increased collisions between the dust and dry surfaces.

Mineral dust could also exert drastic effects on radiative forcing, or changes in atmospheric temperature, and ecosystem survival. In general, atmospheric aerosol can have either net heating or cooling effects, depending greatly on size and physical characteristics (Usher et al., 2003). Furthermore, aerosols often act as cloud formation nuclei, serving as

a seed for droplets to form around. As the amount of dust loading increases, so do the available sites for droplets to form, yielding more and smaller droplets, which are less likely to precipitate, and thus alter rain patterns in certain regions (Buseck et al., 1999). In addition to precipitation scattering, the formation of water droplets on the mineral surface also provides a different chemical interface for reactions to occur. While the dust itself already lent itself for heterogeneous reactivity, adsorbed water introduces the possibility of aqueous chemistry, particularly relevant for SO_2 .

Atmospherically, mineral dusts can also serve as possible sites for hazardous chemicals, organisms, or allergens to adsorb and be transported, leading to propagation of disease and increased allergic reactions. Furthermore, as mentioned earlier, larger mineral aerosol within the PM_{10} range can cause “respiratory damage [as] they penetrate deep into the alveoli of the human lungs, [producing] scarring, and potentially [leading] to conditions such as emphysema” (Usher et al., 2003).

Throughout their time in the troposphere, mineral dusts interact with numerous other atmospheric species, among them inorganic nitrogen and sulfur-based oxide compounds and VOCs, which reside in the atmosphere due to various processes (Usher et al., 2003). Upon exposure to these compounds, mineral dusts can be coated with the reactive species, which change the available sites for reactions to occur through blocking of the surface site or generation of further reactivity with surface adsorbed products. In addition to reacting with VOCs, mineral aerosol can serve as a possible sink and source of compounds such as O_3 , which is associated with high levels of tropospheric pollution.

Field studies evaluating the effect of dust storm events on O₃ concentrations have found that Saharan storms are correlated with between a 5.5-15% reduction of atmospheric concentrations (Soler et. al, 2016). Former chamber studies into the reactivity of O₃ on mineral surfaces have found that O₃ uptake decreases with increased relative humidity and follows a pseudo-first order rate (Cwiertny et al., 2008). This effect can be attributed to the formation of water monolayers on the mineral surface, which compete with the species for reactive site adsorption (Yesilbas et al., 2016). Furthermore, Cwiertny et al. found that O₃ never fully reaches saturation, which indicates the regeneration of surface-site reactivity, characteristic of catalytic processes (2008).

In addition to solid-gas interface reactivity, mineral dust chemistry has intrinsic complexities introduced by atmospheric processing throughout transport. Figure 7 shows some of the forms of processing that dust undergoes while in the atmosphere. One of the least covered to this point is the presence of VOCs from industrial sources and forested areas. Thus, while laboratory experiments often use pure minerals, atmospheric particles often contain organic coatings. These organic coatings introduce a different source of reactivity for atmospheric oxidants, and as such could alter the formation of SO₂ products.

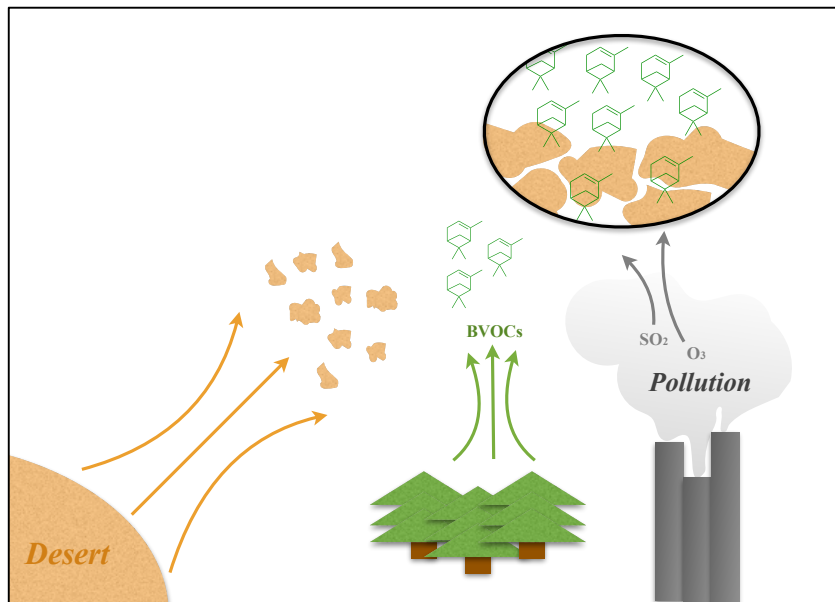


Figure 7. Cartoon representation of the atmospheric processing of mineral dust by biogenic VOCs and pollution. The image shows dust being projected into the atmosphere to form suspended particulates which can be transported over forested regions with high concentrations of aerosolized BVOCs. This will lead to the processing of the dust, as organics coat the surface and react. These processed particles then travel over industrialized areas with high levels of pollution, thus exposing the dust surface to substances like O_3 , NO_2 , and SO_2 .

Current research into the reactivity of mineral dust aerosol has focused on the isolated reactions of trace gases such as O_3 on pure mineral surfaces, primarily involving inorganic species such as NO_2 , $HONO$, N_2O_5 , O_3 , SO_2 , and H_2O_2 , as well as reactive $\bullet OH$ and $HO_2\bullet$ radicals (Romanias et al., 2016). However, as Figure 8 clearly shows, dust from arid regions travels over wide distances covering various forms of terrain. As it is transported from its source region to its final location of deposition, the dust itself undergoes processing which can alter its reactivity with trace atmospheric gases.



Figure 8. MODIS/Terra Normalized Difference Vegetation Index shows land coverage in Asia during October, 2017. Image displays the Gobi Desert in southern Mongolia, the main source region for mineral aerosol affecting the Beijing Tianjin urban region (pink). The orange arrows symbolize possible wind patterns which can transport the dust over forested areas, thus being processed by exposure to biogenic organics. (NASA Neo and Natural Earth for cultural divisions and Jing-Jin-Ji urban area)

In addition to reacting with compounds such as O_3 , mineral dust can interact with VOCs of both biogenic and anthropogenic origins that reside within the troposphere (Usher et al., 2003). Among these organic compounds are a class called terpenes, derived from the dimerization of isoprene, the second most abundant atmospheric hydrocarbon after CH_4 . Two compounds which fall under this category are limonene and α -pinene, used abundantly

throughout the production of home-cleaning products and cosmetics and released through biogenic production from plants:

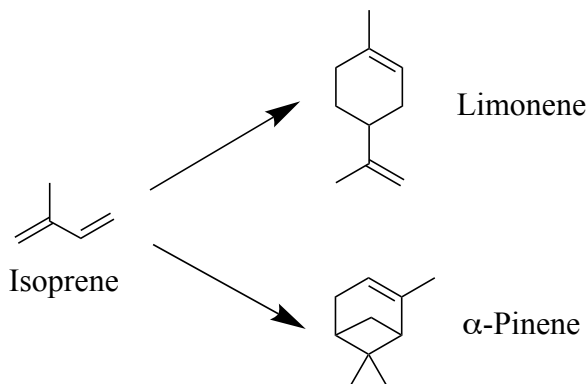


Figure 9. Isoprene and two of its terpene dimers, limonene and α -pinene.

These compounds themselves do not adsorb but have been shown to react with mineral surfaces to produce secondary products which remain adsorbed on the mineral surface, thereby altering the chemical reactivity of the surface (Lederer et al., 2016). In the case of limonene, reactivity with the mineral surface, as seen in Figure 10, yields two main products, limonene diol and carvone, through the reaction with a surface oxygen.

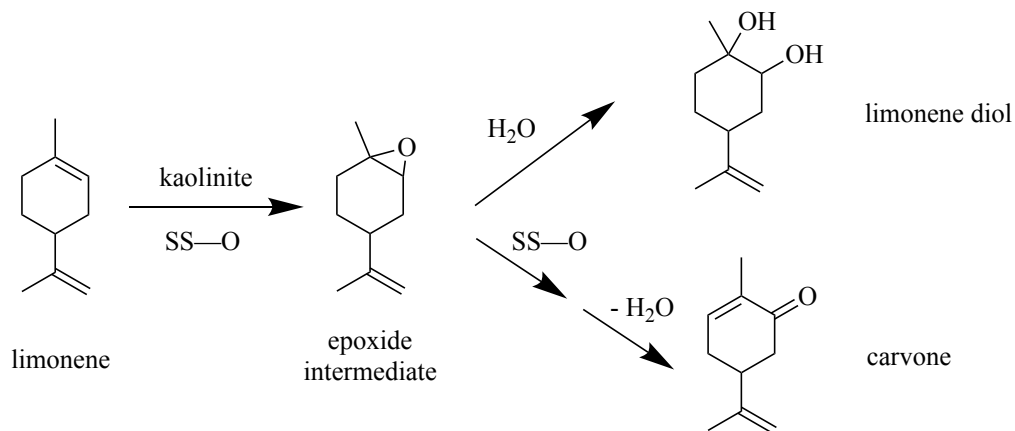


Figure 10. Proposed major reaction scheme for limonene on kaolinite forms limonene diol and carvone. Product formation shows the reaction with a surface

oxygen to form an epoxide intermediate which is then broken open to form its main products: limonene diol (above) and carvone (below) (Lederer et al., 2016).

In the case of α -pinene, reaction with the mineral surface yields α -terpineol which remains adsorbed, as seen in Figure 11.

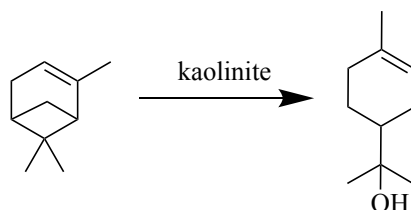


Figure 11. Proposed major reaction scheme for α -pinene on kaolinite forms α -terpineol. Product formation shows the breaking of the bridgehead, a carbocation rearrangement, and a nucleophilic attack to form its main product: α -terpineol (Edziah et al., 2017).

Considering that compounds like O_3 are highly reactive with alkenes, products such as limonene diol and α -terpineol could significantly alter the surface reactivity with O_3 . Furthermore, studies into the reactivity of these VOCs have shown that ozonolysis serves as a major pathway for the decomposition of these molecules within the atmosphere (Grosjean et al., 1993). As such, studies that don't consider processing of mineral aerosol by VOCs may underestimate the actual reaction rates for O_3 decomposition.

1.3 Our Research: Increasing the Complexity of Laboratory Measurements

As noted previously, current lab experiments often focus on the reactivity of pure minerals with trace gases. However, real-world aerosol contain organic coatings due to atmospheric processing by VOCs. Throughout our research, we seek to expand upon current knowledge of specific reactions that occur within the atmosphere in order to provide parameters that can be used to more accurately represent aerosol chemistry in

computational models. Our particular system tests the influence of pollution, land use, and atmospheric conditions on the decomposition of O_3 and SO_2 on mineral dusts. In order to test these variables or influences, we systematically coat a mineral surface by pre-exposing it to limonene and α -pinene. We then compare the reactivity of O_3 and O_3/SO_2 mixes under varying relative humidity (RH).

To test these influences, we measure the uptake coefficients for O_3 decomposition using a laminar flow reactor coupled with an O_3 detector and gas cell, which allow us to detect the O_3 output throughout the reaction. Based on these measurements, we are able to obtain an overall uptake or reaction probability value, which could be inputted into computational models. As seen in Figure 12, we can conceptualize this research as a system with variable input parameters or knobs. By turning on or introducing another variable, we increase the complexity of the experiment and obtain a more accurate uptake value for that reaction. This allows us to evaluate the effect of given variables on the overall reaction probability. This research provides a fundamental understanding of how tropospheric O_3 and SO_2 can be depleted under the presence of processed mineral aerosol. Furthermore, this analysis will provide more accurate parameters for computational models replicating atmospheric chemistry. As such, it could improve the quality of predictions used by policymakers in high-risk areas to enact regulatory policy for atmospheric emissions.

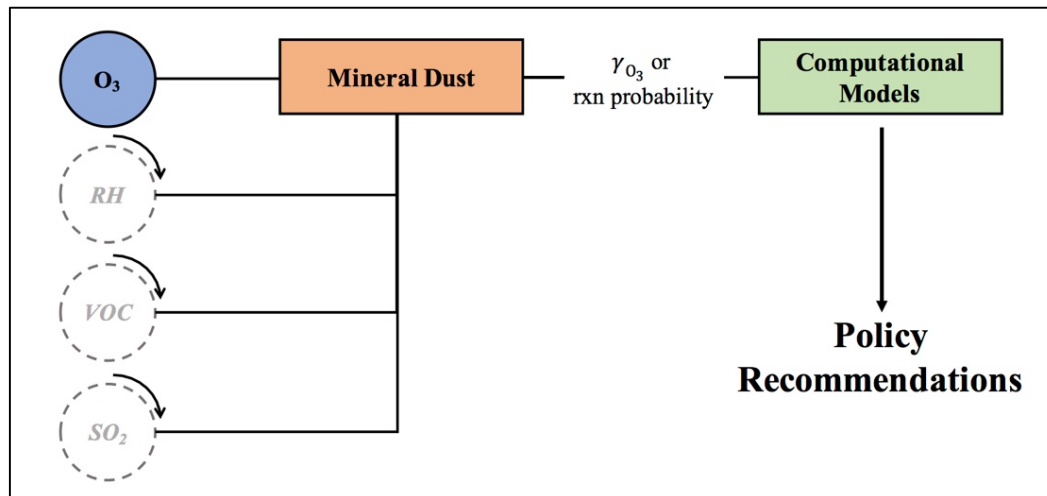


Figure 12. Conceptualization of research variables as knobs that can be turned on or off in order to introduce further complexity to the experiments.

Incorporation of O_3 , RH , $VOCs$, and SO_2 into the experimental procedure alters the reactivity with the mineral dust, thus changing the probability of reaction and the parameters to be inputted into computational models.

Chapter 2: Experimental Methods

The reactivity of atmospheric species on kaolinite, a common component of mineral dust aerosol, was measured using a laminar flow reactor shown in Figure 13, which measures kinetics for heterogeneous reactions involving trace gases and solid surfaces under atmospheric conditions. The setup allows for replicating the atmospheric processing of mineral dusts from arid regions by a variety of species from a chemical perspective. In the present experiments, kaolinite clay was exposed to a constant flow of O_3 and SO_2 , with and without prior exposure to VOCs. By comparing experiments at various relative humidity, we were able to determine the impact of surface adsorbed organics on O_3 and SO_2 reactivity on mineral dust. This chapter provides an overall description of the experimental setup itself, as well as an in-depth explanation of the methods of data analysis and interpretation.

For all experiments, the inner glass tube was coated with kaolinite clay, a common model for dust in the atmosphere, while atmospherically relevant concentrations of O_3 , SO_2 , and VOCs were introduced through the metal insert rod. Exposure of the mineral surface to the insert rod species allowed for the monitoring of concentration changes of gaseous species throughout the experiment. Under constant relative humidity, baseline concentrations of the species in question were monitored. Once the concentration appeared to be stable, first section labeled “A” in Figure 13, the metal insert rod would be retracted, to allow for the species to react with the mineral surface, seen in sections labeled “B” in Figure 13. After 25 minutes of reaction, the rod was reinserted in order to control for variations in species concentration, as seen in the second

portion of “A” in Figure 13. Analysis of this data determined reactive uptake coefficients, which represents the number of reactive collisions between the atmospheric gaseous species and the mineral dust or the probability of reaction occurrence.

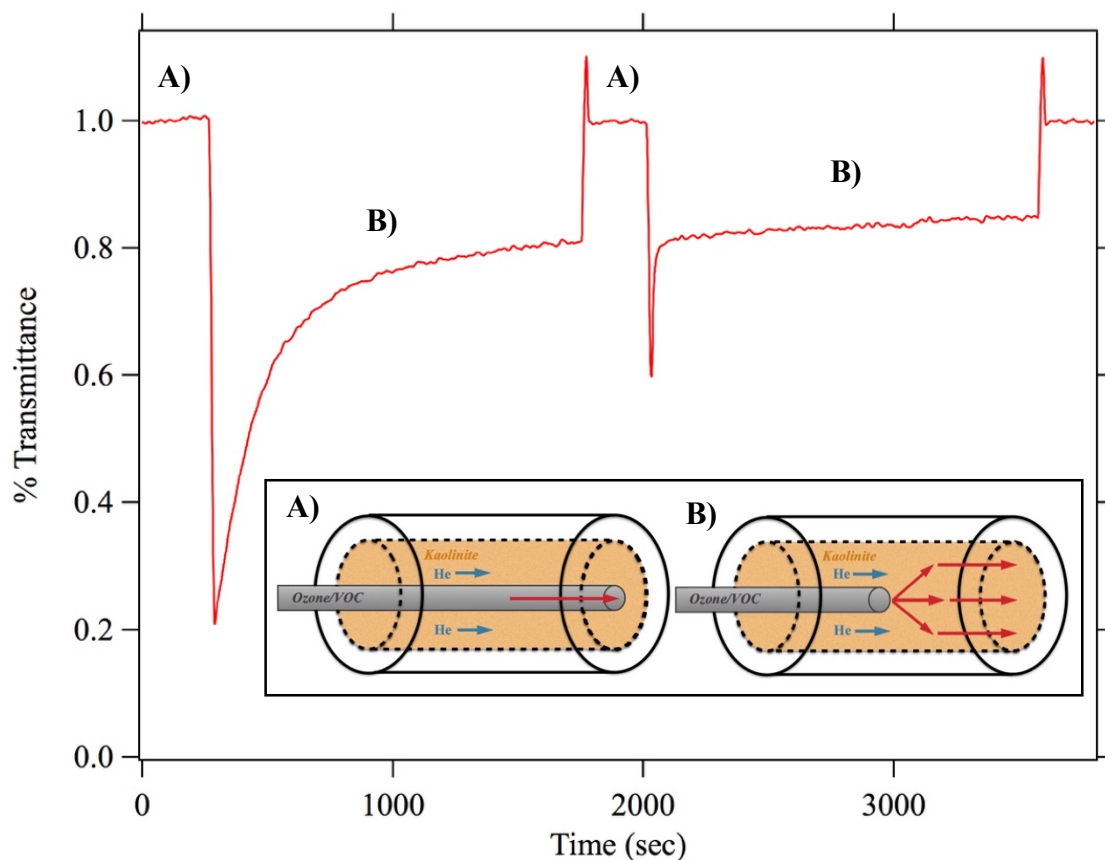


Figure 13. Laminar Flow set-up shows a 122 cm long borosilicate tube, the inner surface of which was coated with a kaolinite–water slurry flowing He as a carrier gas through the outer tube and the reagent in question through the inner metal insert rod. Figure shows reaction tube when collecting baseline concentrations of reactive species (A) for comparison and (B) pulling back of the metal insert rod to allow for reaction between the species and the surface.

2.1 Flow Tube Parameters and Characterization

The main body of the flow reactor consists of a 131 cm long borosilicate tube which holds a 122 cm long (2.43 cm inner diameter) glass insert tube, the inner surface of which was coated with a kaolinite–water slurry (3.5 g of kaolinite, 5.5 g of water) and dried under a continuous flow of helium gas (4 sl/m). Through the inside of the insert tube runs a movable metal injector rod with a constant flow of air carrier gas through which O₃, SO₂, or VOC can be introduced to the flow reactor (1 sl/m). Pulling back of the metal insert rod allows for exposure of the mineral-coated tube to the constant flow of a given reagent, thereby allowing for uptake to occur. Adjustment of relative air flows using Sierra Instruments Digital Mass Flow Controllers (MFC) also allows for changes in RH to account for atmospheric variability. Set-up representation can be seen in Figure 14, with a continuous flow of carrier gases from left to right.

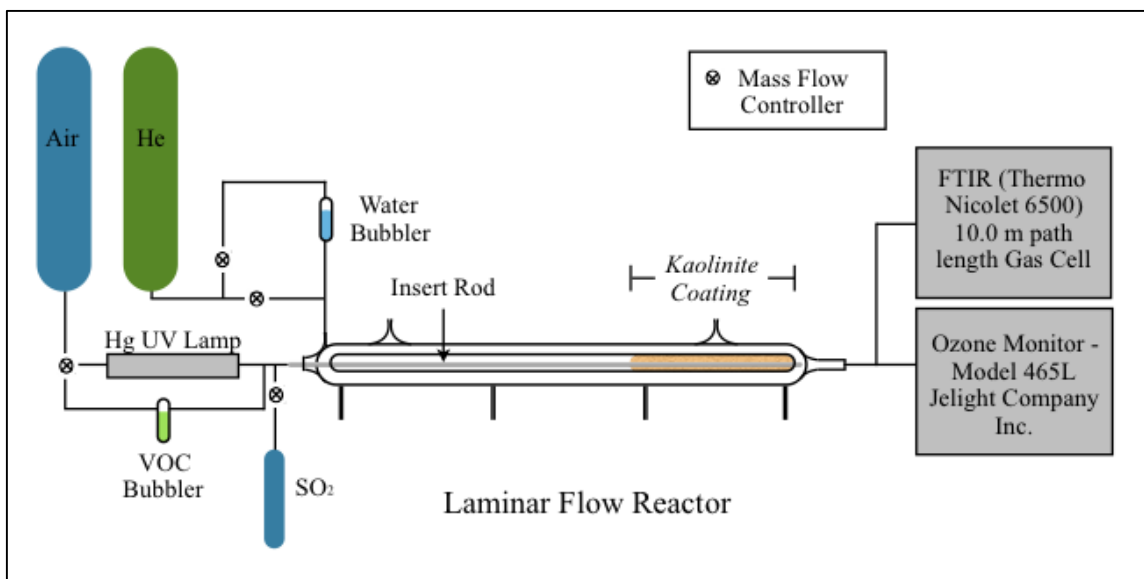


Figure 14. Laminar Flow set-up shows a laminar flow reactor with 20:80 Air/Helium carrier gas and an inner borosilicate glass surface coated with a

kaolinite-water slurry. Manipulation of the air flows and bubbler strengths allows for the measurement of uptake, as seen on the FTIR and Ozone Monitor, as a function of variable RH and surface processing.

Experiments were conducted using kaolinite clay obtained from the Clay Minerals Society's Source Clays Repository. Kaolinite's ($\text{Al}_2\text{Si}_2\text{O}_5(\text{OH})_4$) molecular structure can be seen in Figure 15; it is composed of 2 layers: an octahedral aluminum oxide and a tetrahedral silicon oxide. The clay itself is a high-defect 1:1 phyllosilicate, due to its layered structure, with an elemental composition of 43.9% SiO_2 , 38.5% Al_2O_3 , 2.08% TiO_2 , 0.98% Fe_2O_3 , and 0.15% FeO . In comparison to a pure kaolinite sample which would only contain SiO_2 and Al_2O_3 , this high-defect clay contains titanium and iron based structures within the layers, typically replacing the octahedral aluminum atoms, which introduce variation in available reactivity. Coating of the glass tube was performed using a nylon brush, which yielded a surface coverage of $2.8(\pm 0.5) \text{ mg} \cdot \text{cm}^{-2}$.

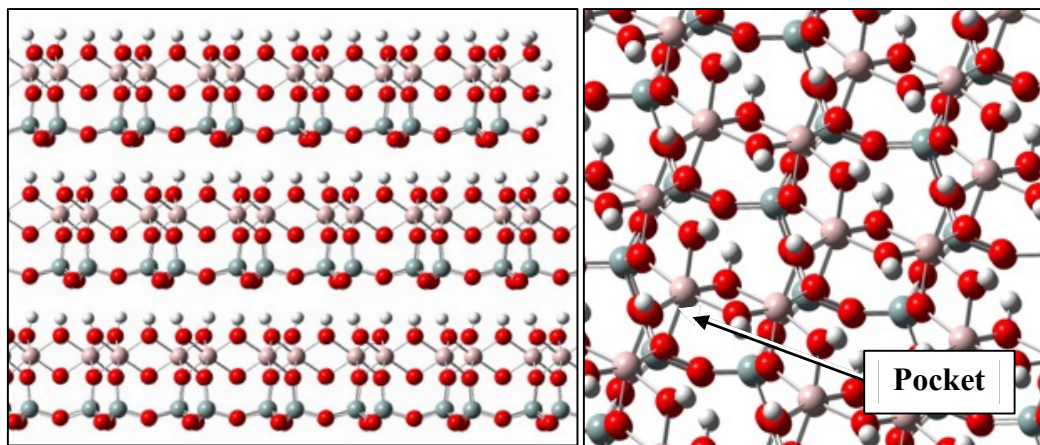


Figure 15. Image shows Gaussian model of kaolinite molecular structure with aluminum (pink), oxygen (red), hydrogen (white), and silicon (gray). The image on the left shows an octahedral aluminum layer above and a tetrahedral silicon layer below. Image on the right shows the molecular structure from above, highlighting

access to aluminum Lewis Acid sites.

Flow tube characterization and determination of laminar flow conditions were done using Knopf et al.'s compilation of equations for flow reactors, sampling tubes, and denuders (2015). Evaluation using our given system's Reynolds (Re) and Peclet (Pe) numbers allowed for an understanding of laminar flow conditions. Re characterizes the flow conditions within the tube, with a low magnitude signifying constant fluid motion (i.e. laminar conditions) and a high magnitude indicating turbulent, variable flow. Evaluation of our setup's Reynolds number, using Eqn. 1, yielded an Re of 58.4. For our setup the flow tube diameter, D_{tube} , was 2.43 cm, the linear velocity v_{g,O_3} was 12.41 cm/s, the dynamic viscosity η was 1.932×10^{-5} kg/m/s, and the carrier gas density δ_g was 0.3741 kg/m^2 , as calculated by the weighted average gas density for our 20:80 Air/Helium air flow (Knopf et al. 2015).

$$Re = \frac{D_{\text{tube}} * v_{g,O_3} * \delta_g}{10000 * \eta} \quad (1)$$

Given that the threshold for laminar flow is set at an Re of 2000, we determined that our system is well within the regime of laminar flow (Knopf et al., 2015).

Based on this determination of laminar flow conditions, we were able to calculate the Peclet number, which designates the ratio of linear transport rate to diffusive transport rate along the axial dimension, calculated using Eqn. 2. For our setup the the diffusion coefficient D_{g,O_3} was $0.46 \text{ cm}^2/\text{s}$, as calculated by the weighted average diffusivity for O_3

in our 20:80 Air/Helium flow. This indicates that the flow along the axis of the flow tube is controlled by the linear flow of the carrier gas and axial diffusion is negligible.

$$Pe = \frac{D_{\text{tube}} * v_{g,O_3}}{D_{g,O_3}} \quad (2)$$

Determination of the distance L to reach laminar flow was calculated using Eqn. 3 and determined to be 4.8 cm. The coating was thereby adjusted so that the inner glass tube was coated with the mineral slurry for 35 cm and the inner metal rod was pulled back 40 cm, allowing for laminar flow to be established before the O₃ comes in contact with the mineral surface, as can be seen in Figure 16.

$$L = 0.035 * D_{\text{tube}} * Re \quad (3)$$

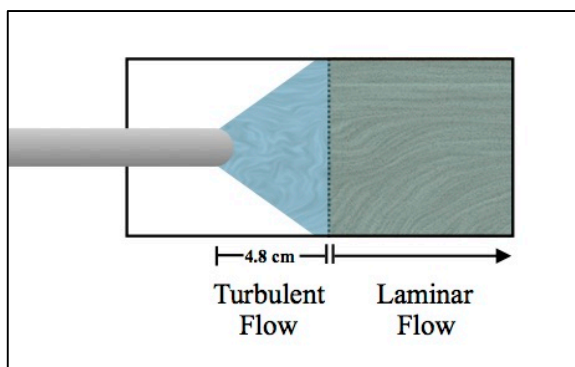


Figure 16. Schematic of flow variations upon exiting inner metal rod. The change in flow dynamics shows that turbulent flow ends and laminar flow conditions are established after 4.8 cm.

The average thermal molecular velocity of O₃ was determined to be 362.8 m/s using Eqn. 4, where ω_{O_3} is the average velocity, R is the Ideal Gas Constant, T is

temperature, and MW represents the molecular weight of O₃ in g/mol.

$$\omega_{O_3} = \sqrt{\frac{8 * R * T}{\frac{MW}{1000} \pi}} \quad (4)$$

For the calculation of the residence time inside the flow tube t , we used Eqn. 6, where l is the length of tube with mineral coating. Residence time for O₃ in our system was determined to be 2.8 seconds.

$$t = l * v_{g,O_3} \quad (6)$$

2.2 Experimental Procedure

2.2.1 O₃ Analysis

The reactive uptake of O₃ on kaolinite was measured using a laminar flow tube reactor coupled with an O₃ monitor (Model 465 L, Jelight Company Inc.). The surface of the inner glass tube was coated with kaolinite-water slurry and dried to 0% RH under a continuous Helium gas flow. After drying, the helium flow was humidified to 0%, 10%, 25%, or 50% by adjusting the relative flow rates of dry and wet helium flows. O₃ was generated using a Hg UV lamp (Jelight) and was consequently introduced in an air carrier gas (1000 sccm) through a movable injector rod (stainless steel) that slides the length of the kaolinite-coated insert tube. When the injector rod was pushed completely forward, the O₃ flow exited the flow tube without interacting with the kaolinite surface and provided a baseline input O₃ concentration, O_{3in}. When the injector rod was retracted to 40 cm, O₃ interacted with the kaolinite surface and the drop in concentration showed the

O₃ being lost to the surface. The combined flow exiting the flow tube passed through an O₃ monitor which monitored O₃ output in the order of parts per billion (ppb), O_{3Out}. The process was repeated several times throughout the experimental run, and the injector rod was re-inserted every 25 minutes to obtain a reference O₃ concentration for data normalization.

Figure 17 shows the reaction progression for O₃ on kaolinite at 0% RH. As can be seen in the figure, the baseline O₃ concentration (O_{3In}) increased slightly throughout the experiment. Since our experiments rely on the assumption that O₃ remains constant throughout the experiment, we account for variability due to setup fluctuations by fitting O_{3In} to a polynomial curve to determine its variability. In light of the fact that O_{3In} determines how much O₃ is going to react, fluctuations in O_{3In} can thus be extended to O_{3Out} measurements as well.

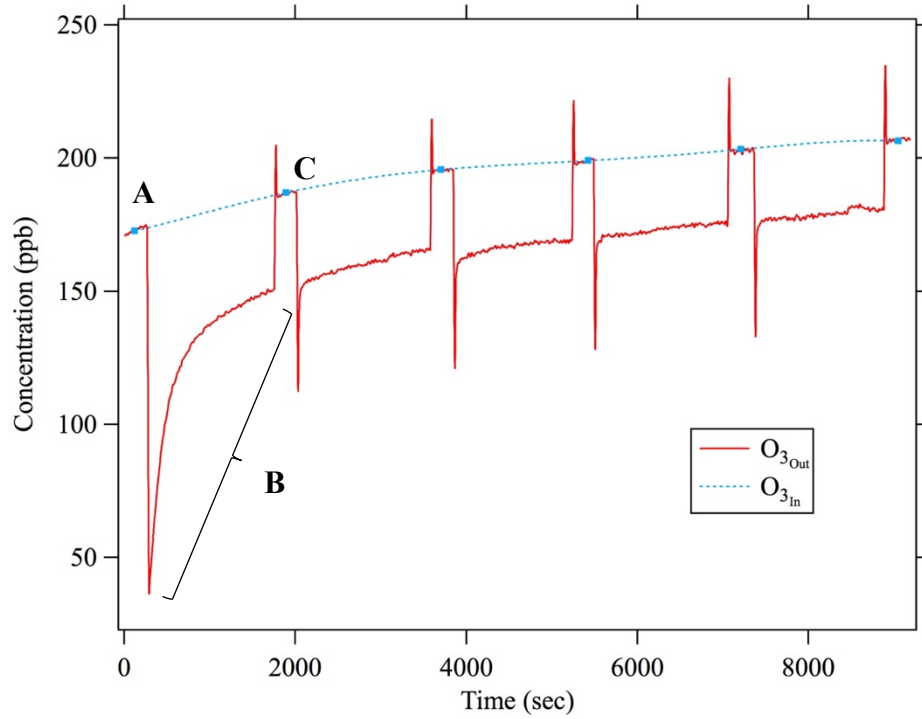


Figure 17. Sample data for variation of O₃ concentration as a function of time when exposed to kaolinite under 0% RH. Graph shows O_{3In} is seen at A. Reaction with kaolinite occurs in region B and region C shows effect of reinsertion of the movable injector rod to obtain the baseline O_{3In}. Polynomial fit (blue) allows for correction of O₃ variability throughout the experiment as a function of O_{3In}.

O₃ concentration throughout the reaction (O_{3Out}) was therefore corrected for O₃ input variability by fitting the data to a polynomial function that describes O_{3In}, as seen in Figure 17 and calculated using Eqn. 7. The order of the polynomial fit varied based on concentration variability.

$$O_{3In} = (k_0 + k_1(\text{Time}_{\text{Total}}) + k_2(\text{Time}_{\text{Total}})^2) \quad (7)$$

O₃ Transmission was calculated using Eqn. 8, where k_i are the fit function coefficients, Time_{Total} is the reaction time, and O_{3Out} is the O₃ concentration measured

by the detector. O_3 Transmission gives us the ratio of O_{3Out} as a function of O_{3In} , which can later be used to evaluate O_3 uptake onto the surface.

$$\text{Transmission}_{\text{Total}} = \frac{O_{3\text{Out}}}{(k_0 + k_1(\text{Time}_{\text{Total}}) + k_2(\text{Time}_{\text{Total}})^2)} \quad (8)$$

Reference concentration time points were removed from the data set and a new continuous time wave was created including data only when reaction was occurring (i.e. when the insert rod was retracted). Effective Uptake Coefficients (γ_{Eff}) for O_3 on mineral dust were calculated using Eqn. 9, where D_{Tube} is the inner tube diameter, ω_x is the thermal velocity of O_3 , t is the residence time, and $\frac{[O_3]_{\text{out}}}{[O_3]_{\text{In}}}$ is the $\text{Transmission}_{\text{Total}}$.

$$\gamma_{\text{Eff}, O_3} = \frac{D_{\text{Tube}}}{(\omega_x t)} * \ln \left(\frac{[O_3]_{\text{In}}}{[O_3]_{\text{Out}}} \right) \quad (7)$$

A sample γ_{Eff} graph for O_3 on kaolinite at 0% RH can be seen in Figure 18. For this graph, γ_{Eff} essentially represents the probability of having a reaction occur between the O_3 and the mineral dust surface. As is clearly shown, the initial exposure of O_3 to the surface has greater probability of reaction due to the wide availability of unreacted surface sites. However, as the time of exposure increases, the probability of reaction decreases, indicating less available sites for reaction. Eventually, the graph shows a stabilization of reactivity known as steady-state reactivity, testifying to the establishment of saturated surface where the rate of the reaction is dependent on the opening up of surface sites as gaseous products are released.

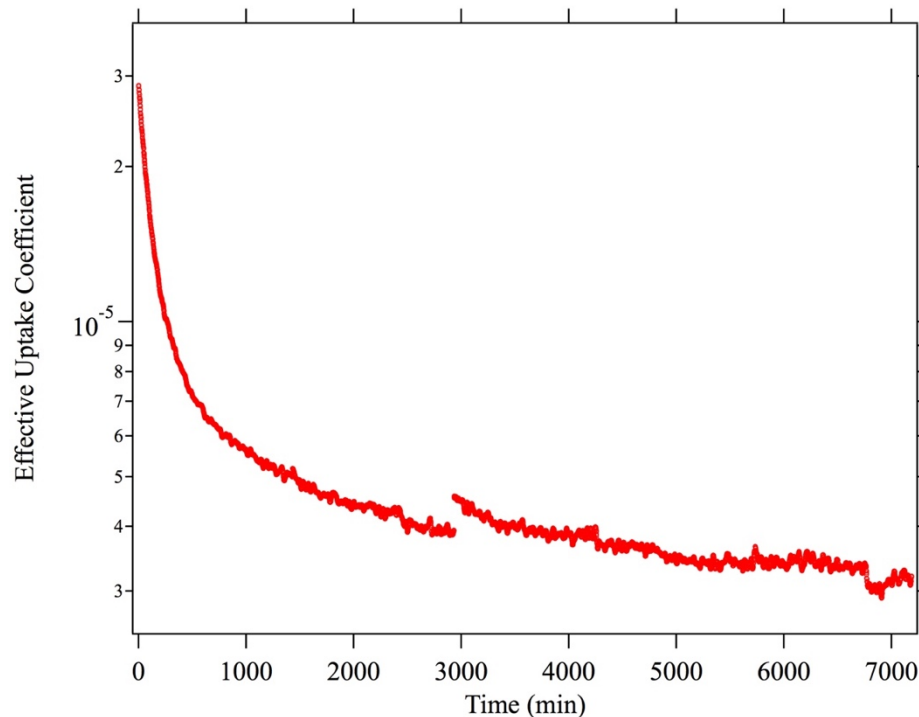


Figure 18. Sample data for $\gamma_{\text{Eff},\text{O}_3}$ of O_3 on kaolinite as a function of continuous time when exposed to kaolinite under 0% RH. Image shows a heightened uptake or reactivity at lower time points and then a stabilization of the reactivity once equilibrium has been attained around 3000 minutes.

Another factor to consider is the effect of very high reactivity on the available concentration of O_3 . Our reaction assumes constant concentrations of O_3 throughout the flow reactor. However, if O_3 is highly reactive with the surface, it may exhaust the available O_3 , creating a gradient of concentration, as is represented through the gas density diagram in Figure 19. In this scenario, the concentration of O_3 would be higher at the center of the tube and would decline as you move outwards toward the kaolinite surface. To correct for this, we calculate the uptake coefficient (γ_{O_3}) using Eqn. 10.

$$\gamma_{O_3} = \frac{\gamma_{\text{Eff},O_3}}{\left(1 - \frac{3}{2} \frac{\gamma_{\text{Eff},O_3}}{N_{\text{Shw}}^{\text{Eff}} Kn_{O_3}}\right)} \quad (10)$$

This parameter shows the actual reactivity, correcting for the set-up's inability to replenish near-surface concentrations of O_3 as quickly as they are being taken up by the surface.

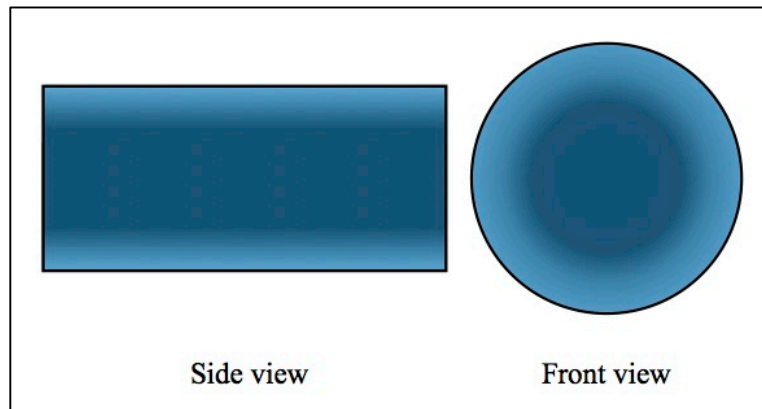


Figure 19. Possible differences in O_3 gas near the surface of the mineral dust for experiments with heightened reactivity. When reactivity is greater than radial diffusion's capacity to replenish consumed O_3 , a concentration gradient is formed.

Figure 20 shows the uptake coefficients before and after considering for radial diffusion. Data show that uptake estimates are more different at lower dose points, particularly when the reactivity is greater. For kaolinite and O_3 , the difference between γ_{Eff,O_3} and γ_{O_3} is relatively small, indicating that the reactivity isn't high enough to cause a significant concentration gradient. As such, there is no need to account for failures in radial diffusion. However, for reactions with heightened reactivity, the differences may be greater, as a gradient is more likely to form. For this graph, the

continuous time variable was normalized for O₃ concentration using Eqn. 11, which yielded a dose measurement in ppb-min.

$$Dose = (Time_{Continuous}) * (Ozone_{In}) \quad (11)$$

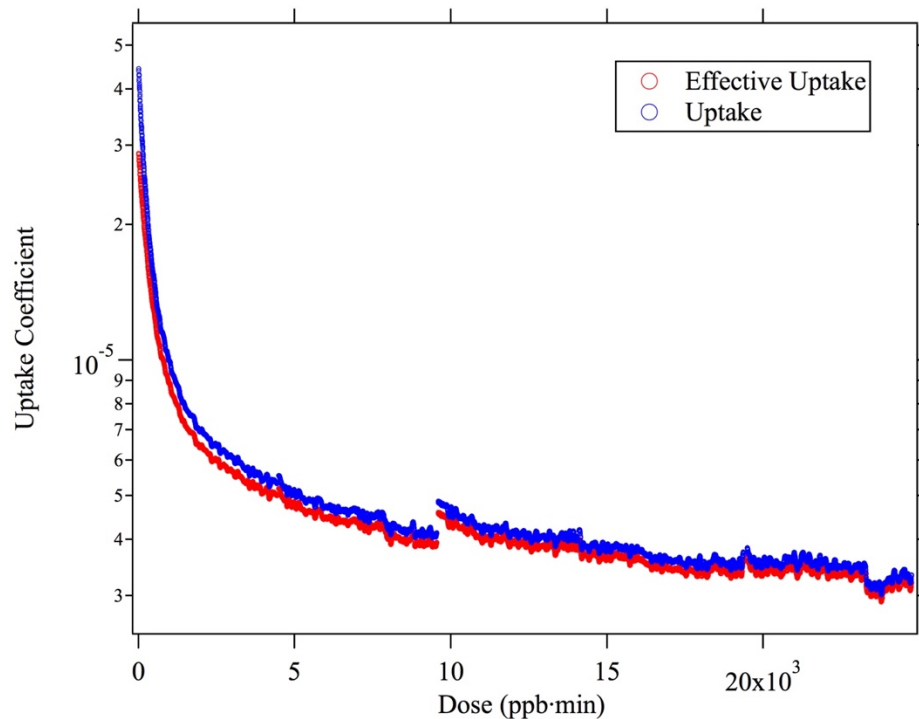


Figure 20. Sample data for γ_{Eff,O_3} (red) and γ_{O_3} (blue) of O₃ on kaolinite as a function of dose, under 0% RH. Graph shows a higher variation between uptake coefficients at lower dose points due to the introduction of radial diffusion by the high rate of reactivity. At lower dose points, the reactivity is more stable and as such the system has more time to regenerate gas-phase concentrations.

Up to this point, calculations have assumed a geometric surface area to the laminar flow setup. This essentially means that the kaolinite coating was assumed to be a flat, perfectly smooth, kaolinite layer. Under this assumption, the available surface area could be calculated using the cylindrical geometry of the tube, seen in Eqn 12, where l is the length of the tube and r is the radius.

$$Area = l * \pi * r^2 \quad (12)$$

However, the kaolinite surface is rough and most likely various layers thick. In fact, measurement of the Brunauer-Emmett-Teller (BET) surface area using a Quantachrome NOVA 2000e Surface Area Analyzer showed that the overall BET area was 242 times larger than the geometric area. This is primarily due to the fact that the kaolinite coating is uneven, as depicted in Figure 21, and thus allows for gaseous compounds like O_3 to react within interior crevices and imperfections.

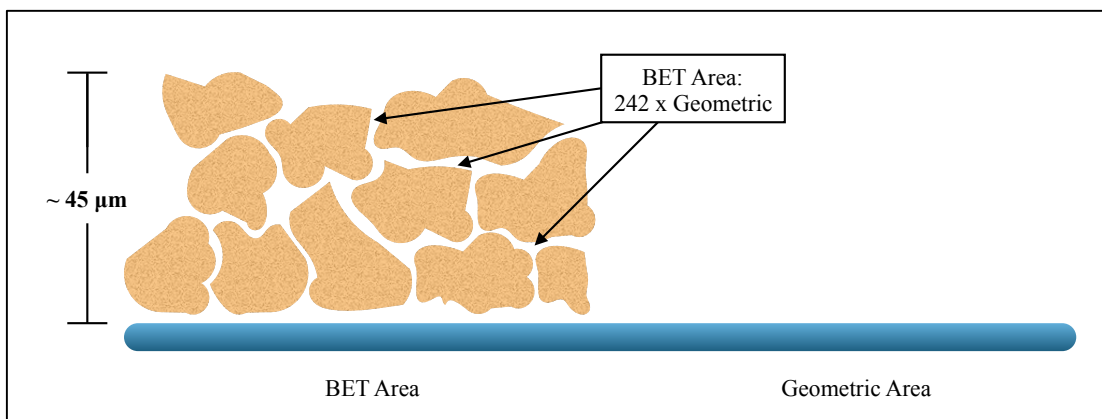


Figure 21. Reactive surface area based on BET calculations. Model shows that there are 242 times more available surface sites in the BET area (left), coated with mineral dust, when compared to the geometric surface (right), uncoated. This means that O_3 has significantly more sites to react with and adsorb to, and as such, the measurements taken previously over-estimated O_3 -kaolinite reactivity by two orders of magnitude.

This increased understanding of available surface means that all previous uptake calculations based on geometric surface area over-estimate reactivity by approximately 242 times. For this reason, we corrected the γ_{O_3} for BET surface area by dividing by 242,

which yielded the values presented in Figure 22, showing a decrease in observed reactivity by two orders of magnitude.

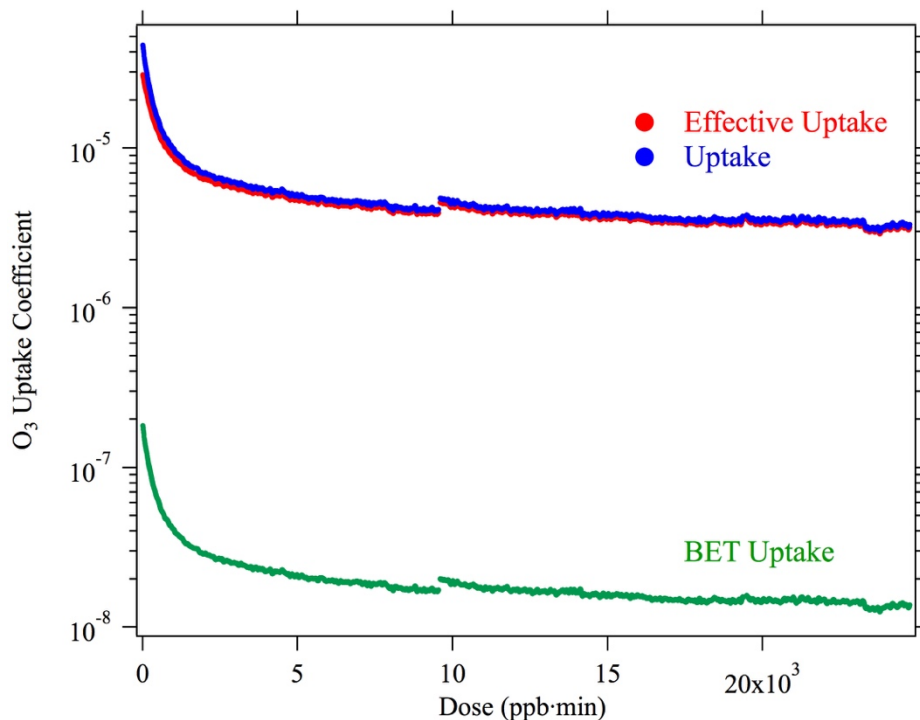


Figure 22. Sample data for $\gamma_{\text{Eff},\text{O}_3}$ (red), γ_{O_3} (blue), and $\gamma_{\text{BET},\text{O}_3}$ (green) of O_3 on kaolinite as a function of dose, under 0% RH. Shows two order of magnitude decrease in reactivity when comparing BET-corrected (non-geometric) uptake to geometric surface area uptake.

Accounting for the BET or actual surface area provides the most accurate measurement of surface reactivity. For this reason, all subsequent data will be presented and analyzed as a function of γ_{BET} .

2.2.2 VOC Processing of Kaolinite

The main objective of this research is to increase the complexity of atmospheric models in order to better represent the chemistry of atmospheric mineral dust. Thus, pure minerals do not provide an accurate representation of reactivity, since they do not account

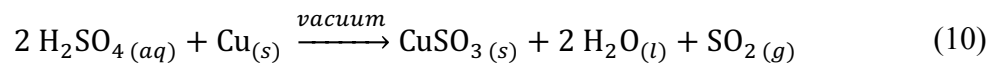
for various forms of atmospheric processing by compounds originating from forested and industrial regions. In order to replicate VOC chemistry on the mineral dust, we selected two mono-terpenes, limonene and α -pinene, due to their known chemical reactivity.

The reactive uptake of O_3 on kaolinite was also measured as a function of VOC coating and SO_2 exposure. For the VOC experiments, the kaolinite surface was coated with VOC under humidified conditions for a total of 10-15 minutes before exposing the surface to O_3 . The VOC flow exiting the flow tube passed through a 10-m path length FTIR gas cell that monitored the VOC concentration (4 cm^{-1} resolution, 16 scans, 0.26 min averaging). Comparison of the VOC concentration with the injector rod pulled back relative to being pushed forward allowed for measurement of the transmission of VOC through the kaolinite-coated tube. This experiment was run at variable humidity with limonene and α -pinene. For the SO_2 experiments, ~ 7 sccm of SO_2 were combined with 994 sccm of O_3 upstream of the coated tube. Uptake of SO_2 by the surface was also measured using the FTIR gas cell.

2.2.3 SO_2 Synthesis

Another objective of this research is to understand possible pathways of SO_2 oxidation, as a means to determining sulfate formation in regions of high pollution. Most literature studies have developed gas-phase and liquid-phase mechanisms of SO_2 oxidation. However, we seek to evaluate mineral dusts as a possible interface for SO_2 oxidation, either through the formation of a liquid layer that allows for liquid-phase-like mechanisms or through solid-gas interface reactivity.

For experiments testing the reactivity of SO₂, a stock of SO₂ was synthesized using a vacuum manifold and kept under vacuum for future experiments. For synthesis, concentrated sulfuric acid was degassed and purified using multiple freeze-pump-thaw cycles, copper turnings (~1 g, 63.5 mol) were added under N₂ gas into the reaction bulb connected to the gas manifold. The bulb was then evacuated and kept under vacuum throughout the reaction process seen in reaction 10.



The temperature of the reaction mixture was raised to ~108-120 °C and product formation was monitored through changes in manifold pressure using a pressure gauge. The product was collected in the gas phase using the manifold, diluted with N₂ gas, and stored in a 5 L glass bulb for future transfer into a lecture bottle. Gas cell IR spectra corroborated the formation of SO₂ when compared to Pacific Northwest National Lab (PNNL) infrared database (Major IR peaks: 1150 cm⁻¹, 1360 cm⁻¹, 2500 cm⁻¹).

2.2.4 SO₂ Analysis

Concentrations of SO₂ were determined by comparing absorbances for our infrared spectra to the Pacific Northwest National Lab (PNNL) infrared database, as seen in Figure 23. However, PNNL uses scan resolutions of 0.125 cm⁻¹, which allow for a more accurate measurement of rotational vibrational features, as lower resolution spectra don't show all of the molecular energy transitions, but rather represent an average measurement. Thus, since all our experimental spectra are taken at a resolution of 4. cm⁻¹, we needed first determine the conversion factor between our spectra at 4. cm⁻¹ and the

spectra 0.125 cm^{-1} . This comparison allowed us to correct variations in our setup's measurements of SO_2 , yielding a more accurate concentration value.

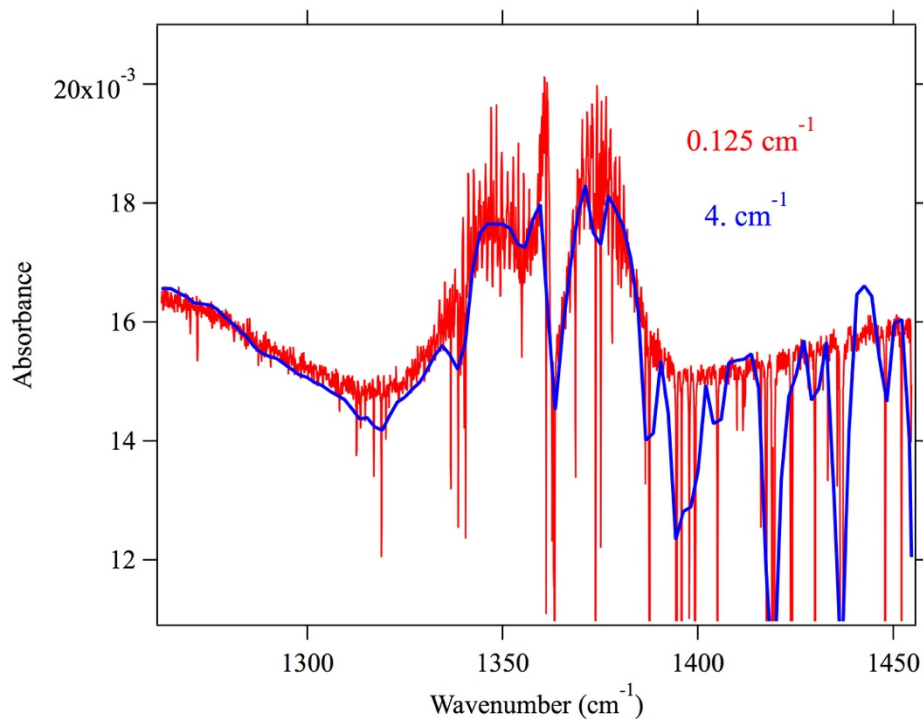


Figure 23. Gas cell infrared spectra of SO_2 at 0% RH using 0.125 cm^{-1} (red) and $4. \text{ cm}^{-1}$ (blue) resolutions. Spectra show the highest absorbance around 1360 cm^{-1} for experimental concentrations of SO_2 . At higher resolutions, greater spectral resolution and details are visible.

Beer's Law was used to calculate overall SO_2 concentration in the system, as seen in Eqn. 13, with Abs indicating peak intensity, σ_{SO_2} being the molar absorptivity of SO_2 , and l representing the gas cell path length. For the PNNL database, reported σ_{SO_2} was $8.0 \times 10^{-2} \text{ ppm}^{-1} \text{ m}^{-1}$.

$$[\text{SO}_2] = \frac{\text{Abs}}{\sigma_{\text{SO}_2} * l} \quad (13)$$

Thus, the SO₂ signal in Figure 23 was found to be ~432 ppb. Comparison to the 4 cm⁻¹ SO₂ spectrum showed that this concentration was equivalent to an integrated peak area of 0.0658589 for the peak at 1320-1390 cm⁻¹, which allows for the calculation of a conversion factor, as seen in Eqn. 14, to be used in experimental SO₂ concentration calculations in further experiments.

$$\text{Conversion Factor} = \frac{432}{0.0658589} \quad (14)$$

Integrated peak area was selected as the method for correlation in order to account for the complexities of the vibrational frequency. If only peak height were used, it would provide a less comprehensive analysis of the signal.

Since water vapor, which is present at high RH, overlaps the SO₂ vibrational features, we need to subtract H₂O features to accurately measure SO₂. Figure 24 shows certain regions of vibrational frequency overlap.

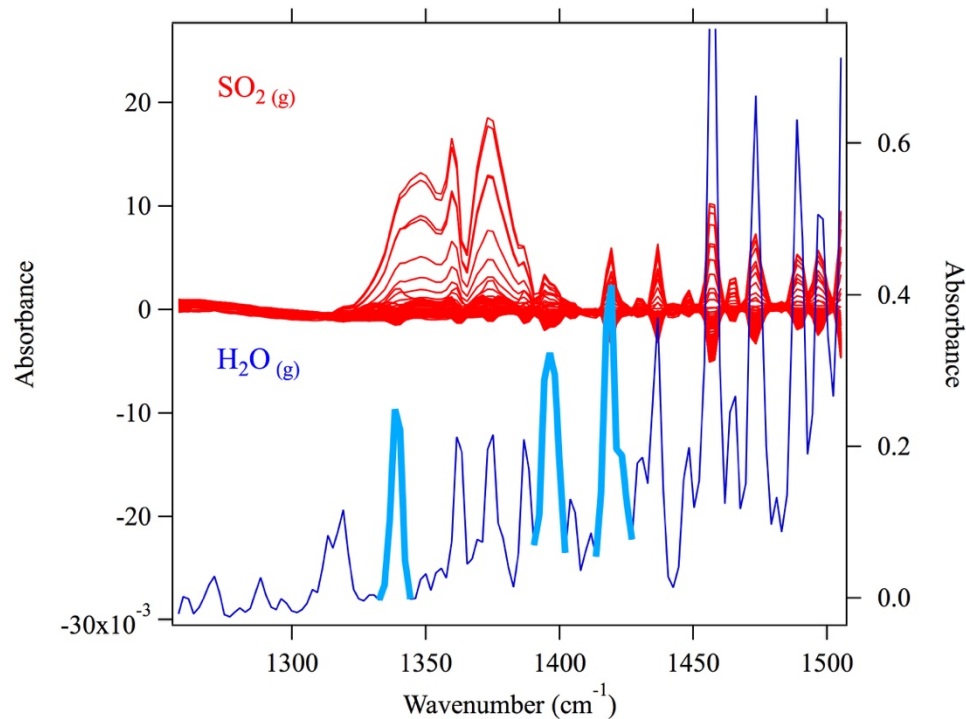


Figure 24. Gas cell infrared spectra of SO₂ throughout the reaction progression at 4. cm⁻¹ resolutions (red, axis left) with an overlaid spectrum for pure gas-phase water (blue, axis right). Spectra show water interference with SO₂ vibrational frequencies, thus making it necessary to perform a water subtraction on the SO₂ data to account for noise due to the relative humidity. Light blue lines show main reference peaks used for water vapor subtraction.

After subtracting the H₂O interference from the SO₂ raw data, we are now able to integrate the overall peak area for SO₂, between 1324.9 cm⁻¹ and 1392.4 cm⁻¹, to determine the concentration. Since spectra are recorded continuously every 3 minutes, we can use this data to determine SO₂ transmission as shown in Figure 25. Integrated area can then be converted to ppb concentrations using the conversion factor obtained in Eqn. 14. Having obtained this basic concentration data, we are able to analyze the results in the

same fashion as the O_3 data above, obtaining SO_{2In} , SO_{2Out} , $\gamma_{[SO_2]}$, and dose for each experiment.

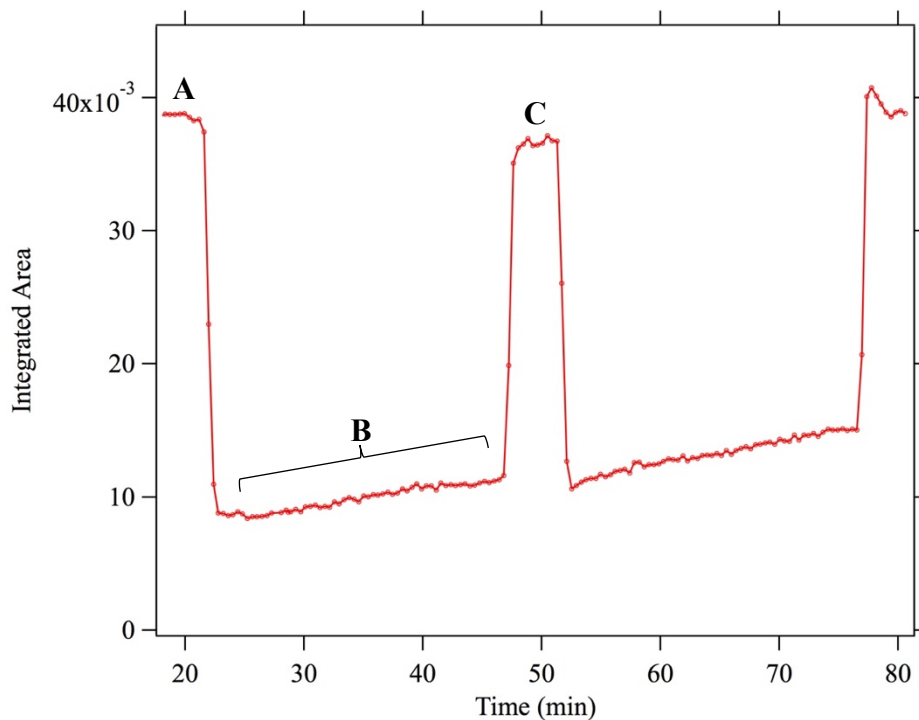


Figure 25. Sample data for SO_2 integrated area as a function of time when exposed to kaolinite under 25% RH; fitting of insertion points to a polynomial yields SO_{2In} . Graph shows SO_{2In} is seen at A. Reaction with kaolinite occurs in region B and region C shows effect of reinsertion of the movable injector rod to obtain the baseline SO_{2In} .

Chapter 3: Results and Discussion

Throughout our research, we seek to expand upon current knowledge of specific reactions that occur within the atmosphere in order to provide parameters that can be used to more accurately represent aerosol chemistry in computational models. Consequently, our experimental system tests the influence of pollution, land use, and atmospheric conditions on the decomposition of O₃ and SO₂ on mineral dusts. However, in order to fully understand the complexities of mineral dust chemistry, it is necessary to characterize reactivity of each facet independently, and then test it in a system with multiple variables.

To test these influences, we measure the uptake coefficients for O₃ decomposition using a laminar flow reactor coupled with an O₃ detector and gas cell, which allow us to detect the O₃ output throughout the reaction and evaluate the reactivity on the mineral dust surface. This chapter provides a comprehensive explanation of our research process by examining each intervening variable in the larger chemical system. Throughout the chapter I will explain O₃ reactivity on pure kaolinite, under variable RH, on VOC-processed mineral dust, under various O₃ concentrations, and finally with respect to SO₂ exposure.

3.1 Reactivity of O₃ on Pure Kaolinite

Most literature studies analyzing the complexities of mineral dust in the atmosphere have evaluated the reactivity of the dust in its pure form. For this reason, we first tested the reactivity of pure kaolinite in order to place it within the context of mineral dust literature. This allows us to compare our results to prior work in order to corroborate the validity of our system.

In order to begin the discussion of variables that affect O₃ reactivity on mineral dust, we first need to evaluate the baseline reactivity of O₃ as evaluated in the literature. When testing O₃ uptake at 0% RH, the data show a high initial $\gamma_{\text{BET},\text{O}_3}$ of approximately 1.83×10^{-7} , with a rapid decrease until a near steady state is achieved, as seen in Figure 26. Comparison of the initial reactivity to the stabilized $\gamma_{\text{BET},\text{O}_3}$ appears to indicate the passivation of reactive surface sites, considered near steady state reactivity. Most laboratories currently report their values for initial uptake, which show a heightened reactivity of O₃ with the surface. However, steady-state reactivity may be more representative of atmospheric chemistry. For this reason, the values we report are averages of the $\gamma_{\text{BET},\text{O}_3}$ for 4,000 to 10,000 ppb·min, a dose range where near steady state has been achieved.

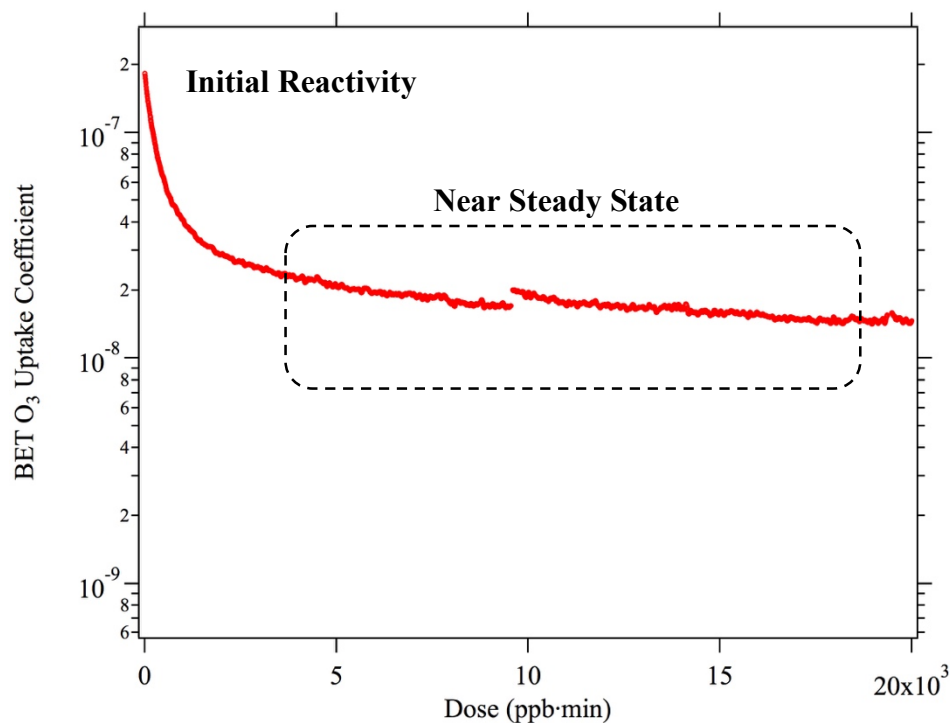
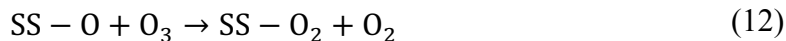


Figure 26. $\gamma_{\text{BET},\text{O}_3}$ on kaolinite as a function of O_3 -normalized time (dose) when exposed to kaolinite at 0% RH. The slope of the curve indicates greater reactivity at earlier dose points, with a stabilization or steady state around 4,000-10,000 ppb-min. This shows a plateau in reactivity, indicating an equilibrium between adsorption and desorption based on SS.

Reactivity for kaolinite at 0% displayed an initial $\gamma_{\text{BET},\text{O}_3}$ of 1.83×10^{-7} , and a near steady state average $\gamma_{\text{BET},\text{O}_3}$ of 1.92×10^{-8} . This comes in contrast to literature values of initial and steady state uptake of 10^{-4} and 10^{-5} , respectively (Karagulian and Rossi, 2005). However, they are comparable to initial $\gamma_{\text{BET},\text{O}_3}$ values on $\alpha\text{-Al}_2\text{O}_3$ of 1.4×10^{-7} and 8.0×10^{-8} (Roscoe and Abbatt, 2005) as well as Mogili et al.'s $\alpha\text{-Fe}_2\text{O}_3$ $\gamma_{\text{BET},\text{O}_3}$ in the order of magnitude of $\sim 10^{-7}$ (2006). Mogili et al. also contrast their variable $\gamma_{\text{BET},\text{O}_3}$ numbers in reference to their sample analysis setup. In the case of their Knudsen cell study of $\alpha\text{-Fe}_2\text{O}_3$ reactivity, they found $\gamma_{\text{BET},\text{O}_3}$ in the order of magnitude of 10^{-4} (2006), which is consistent with Karagulian and Rossi's results, also collected at low pressure in a Knudsen cell reactor (2005). Having accounted for pressure dependence variations, updated initial $\gamma_{\text{BET},\text{O}_3}$ values largely show magnitudes of $\sim 10^{-7}$, which are consistent with our results (Cwiertny et al., 2008).

This decrease in O_3 reactivity at lower times is consistent with reactions 11a, 12, and 13 below, where SS represents the reactive surface site on kaolinite. In the reaction process, O_3 adsorbs to the reactive SS, splitting into an adsorbed reactive oxygen and releasing gaseous O_2 . The reactive oxygen can then further react with other incoming O_3 , reaction 12, or other adsorbed oxygens, reaction 13.



This process is consistent with the data observed in Figure 25, which shows the $\gamma_{\text{BET},\text{O}_3}$ as a function of dose, with high initial reactivity as O_3 adsorbs to surface sites and reacts. However, as time progresses, surface sites become saturated with O_2 , thereby decreasing the available points of reaction. This would seem to indicate that reaction 14, where O_2 molecules desorb to regenerate the surface site, is a slow process.



Having reached the steady state equilibrium, visible through a constant slow uptake, the rate of desorption of the adsorbed O_2 is determining the availability of surface sites for reactions to occur (Karagulian and Rossi, 2005). Some studies looking into the effect of particle mineralogy on reactivity have found that the rate of reaction 12 is related to the strength of the interaction between the surface site and O_2 . The more electrophilic the metal, based on its electronegativity and size, the more favorable the interaction with the O_2 electrons. This helps to explain why dusts with strong Lewis Acid sites such as $\alpha\text{-Al}_2\text{O}_3$ saturate more quickly and become unreactive in comparison to dusts like $\alpha\text{-Fe}_2\text{O}_3$, which readily frees its O_2 from binding interactions due to its weaker acidity (Cwiertny et al., 2008).

Further studies into O_3 's reactivity with various dusts demonstrated that, under dry conditions, $\alpha\text{-Al}_2\text{O}_3$ has an initial uptake coefficient of 3.5×10^{-8} , while $\alpha\text{-Fe}_2\text{O}_3$ has an uptake coefficient of 1.0×10^{-7} , corroborating the expected differences in surface reactivity

due to Lewis acid site affinity. Moreover, α -Fe₂O₃ followed a catalytic behavior of surface site regeneration, while α -Al₂O₃'s surface saturated at a given O₃ concentration due to stronger interactions between the SS and the adsorbed products (Mogili et al., 2006).

3.2 Determination of the Relative Humidity Dependence of O₃ Uptake

Given the prevalence of water within atmospheric chemistry, it is necessary to evaluate the effect this water has on surface reactivity. Numerous studies have looked into the adsorption of water onto mineral dust surfaces as a function of relative humidity (Ma et al., 2010; Yesilbas and Boily, 2016). They have found that as RH increases, water adsorbs onto the mineral surface through a multitude of interactions, among them hydrogen bonding with hydroxyl groups on the dust surface. Furthermore, as RH increases, water follows a sigmoidal trend in adsorption onto the surface, showing the formation of layers with varying thicknesses and structures (Yesilbas and Boily, 2016). As reported by Cwiertny et al., for RH values exceeding 10%, water forms thin films or monolayers which vary in quantity with increased humidity (2008). This, in turn, introduces a different component into the reactivity with surface sites. While some sites may be blocked by water molecules, the formation of a water monolayer allows for possible dissolution of compounds and the occurrence of liquid-phase chemistry at the surface. Furthermore, Figure 27 shows the possibility of water forming in a quasi-liquid layer which still leaves open surface sites for reactivity.

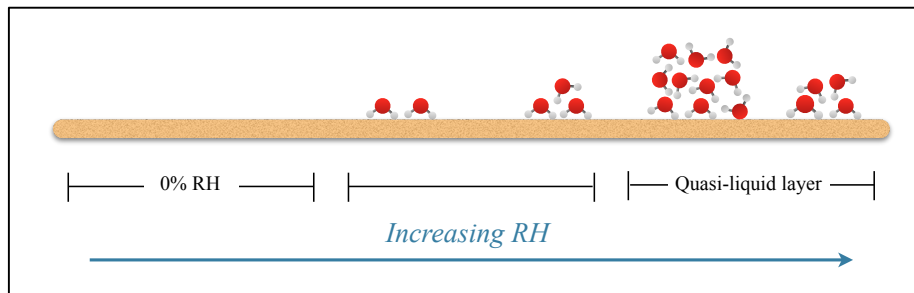


Figure 27. Water adsorption onto the mineral dust surface as a function of increasing relative humidity. Diagram shows the increased adsorption of water onto the surface with increased RH. However, the water does not necessarily form a uniform monolayer, as described in the literature, but could instead accumulate in a quasi-liquid layer with patches of uncovered mineral surface.

For this variable, laminar flow reactor experiments quantify the $\gamma_{\text{BET},\text{O}_3}$ of O_3 on kaolinite at approximately 0%, 10%, 25%, and 50% RH, as a measure of the availability of surface sites for the reaction progression. As seen in Figure 28, when RH is increased, $\gamma_{\text{BET},\text{O}_3}$ shows a downward shift by approximately an order of magnitude, or 10 times. This is an indication of overall decreased reactivity, as the probability of having a reaction occur, $\gamma_{\text{BET},\text{O}_3}$, is lower. In light of this, we can interpret the results to mean that some form of reactive inhibition or competition is taking place.

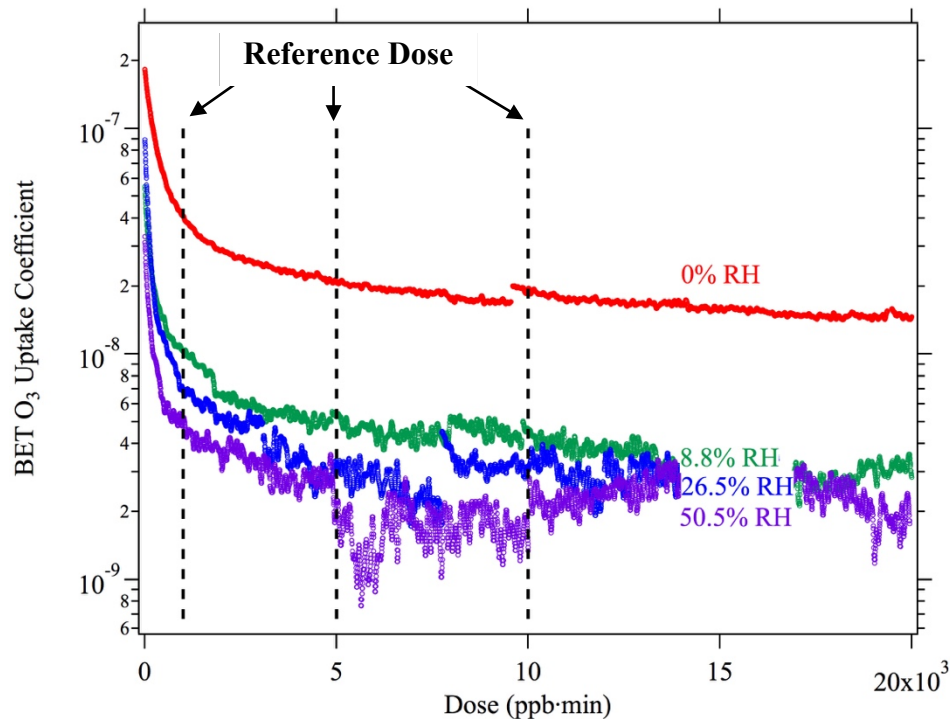


Figure 28. $\gamma_{\text{BET},\text{O}_3}$ on kaolinite at 0, 8.8, 26.5, and 50.5% RH as a function of dose. The steady state reactivity at higher RH shows an order of magnitude decrease from that of 0%. Since the $\gamma_{\text{BET},\text{O}_3}$, or the probability of having a reaction occur, is lower, this indicates some form of reaction inhibition. Vertical dashed lines show dose points selected for dose comparison.

In a manner consistent with the literature, our data show a decrease in uptake of O_3 at higher RH, as seen in Table 1. More specifically, average $\gamma_{\text{BET},\text{O}_3}$ for 0% RH is $1.92 (\pm 0.16) \times 10^{-8}$. However, when exposed to different RH's, the average $\gamma_{\text{BET},\text{O}_3}$ decreases to $4.64 (\pm 0.40) \times 10^{-9}$, $2.95 (\pm 0.49) \times 10^{-9}$, and $1.88 (\pm 0.54) \times 10^{-9}$ at 8.8%, 26.5% and 50.2% RH, respectively. In order to analyze the effect of RH on different time points along the reaction progression, we take the reference dose points marked in Figure 28 and evaluate their respective $\gamma_{\text{BET},\text{O}_3}$, as seen in Figure 29. Figure 29 shows a decrease in reactivity at higher RH for all dose points. Moreover, a comparison of the

1000 ppb-min, or initial, variability to the steady state reactivity shows a dramatic difference, particularly at lower RH values. Furthermore, the leveling off of reactivity after 25% for steady state corroborates our assumption that higher RH values than tested by our experiments would produce similar trends to our upper limit RH values.

Table 1: Average steady state BET uptake coefficients for O₃ at varying RH

	RH			
	0%	8.8%	26.5%	50.5%
$\gamma_{\text{BET},\text{O}_3}$	$1.92 (\pm 0.16) \times 10^{-8}$	$4.64 (\pm 0.40) \times 10^{-9}$	$2.95 (\pm 0.49) \times 10^{-9}$	$1.88 (\pm 0.54) \times 10^{-9}$

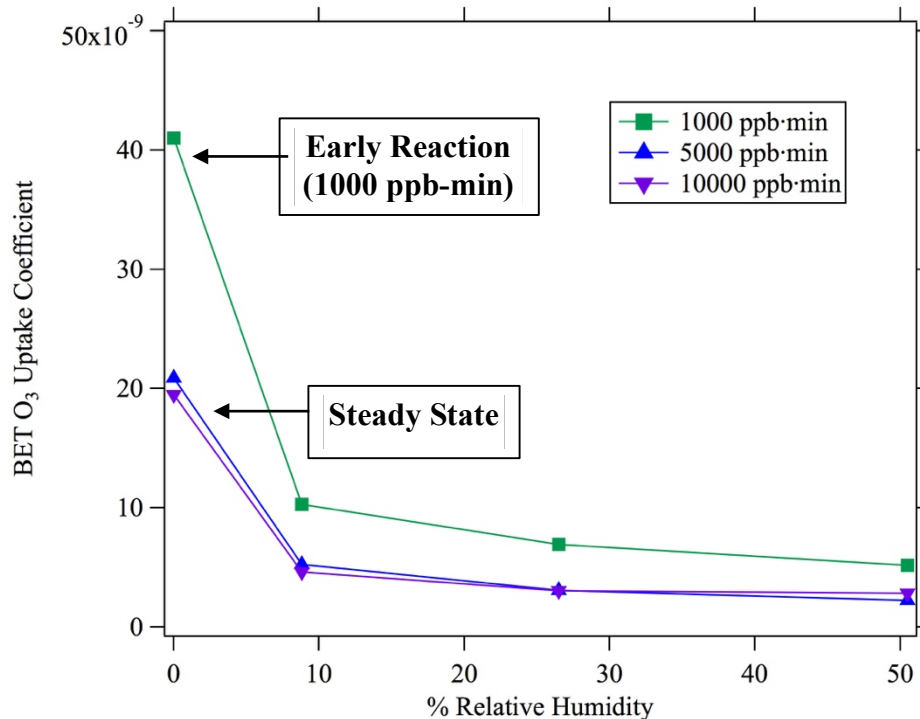
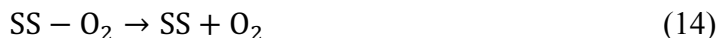
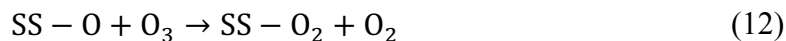


Figure 29. $\gamma_{\text{BET},\text{O}_3}$ O₃ on kaolinite at 0, 1000, 5000, and 10000 ppb-min as a function of RH. The stabilization after ~10% RH for steady state reactivity indicates that RH-dependence is constant after a threshold and thus can be extrapolated to higher RH values.

The drastic decrease in surface reactivity at higher humidity is consistent with competitive adsorption onto the dust surface, where O_3 is unable to adsorb to the reactive sites due to a water monolayer. This can be seen more clearly through the proposed mechanism of dissociative adsorption for O_3 on kaolinite's SS, described in reactions 11-14. For this reaction mechanism, schemes 11a, 12, and 14 represent the adsorption, reaction of surface adsorbed O, and regeneration of the SS through the release of O_2 , respectively. However, pathway 11b represents the adsorption of water onto the mineral surface, which creates an alternative to the binding of O_3 , and therefore follows a competitive adsorption model. However, despite the decrease in uptake, a non-zero steady state reactivity at high RH is still seen, which suggests that not all surface reactivity is lost to this alternative pathway.



In their DRIFTS-FTIR study into the reactivity of O_3 on alumina, Roscoe and Abbatt found that oxygen species formation on the alumina from adsorbed O_3 slowed almost completely after 20% RH (2005). They hypothesized that the decrease in products could be either due to competitive adsorption of the water onto the Lewis Acid sites on the surface that serve as primary points for O_3 adsorption or from water driving off the adsorbed products from the surface due to the system setup. In their system, O_3 reactivity

was monitored under 0% RH, then the system was exposed to water vapor to determine changes in adsorbed species. They found that exposing the surface-adsorbed oxide products to water vapor led to a decrease in products and an increase in adsorbed water, hinting at the displacement and inhibition of formation of oxide species in favor of SS-water interactions (2005). Mogili et al. similarly find that increasing the RH decreases the uptake of O₃, however, for lower RH values where water coverage is below one monolayer, SS's were not saturated on α -Fe₂O₃ (2006).

Fourier transform infrared spectrometry (FTIR) studies into the number of monolayers formed at a given relative humidity found that at an RH of 10%, approximately 1-1.5 layers of water are formed, whereas at 25% and 50%, water forms 2 and 3 layers, respectively (Cwiertny et al. 2008). From 0% to 25% $\gamma_{\text{BET},\text{O}_3}$ decreases by approximately a factor of ten. In contrast, the transition from 25% to 50% shows a halving of the rate. This introduces the possibility that the layers may not form as an even coat throughout the surface, but rather aggregate in small puddles, leaving reactive surfaces on the dust without competitive adsorption. Moreover, it is possible that dissolution of the O₃ into the liquid layer introduces additional liquid-phase pathways for decomposition, as determined by Henry's law coefficient for the diffusion of O₃ into water, seen in Figure 30 below.

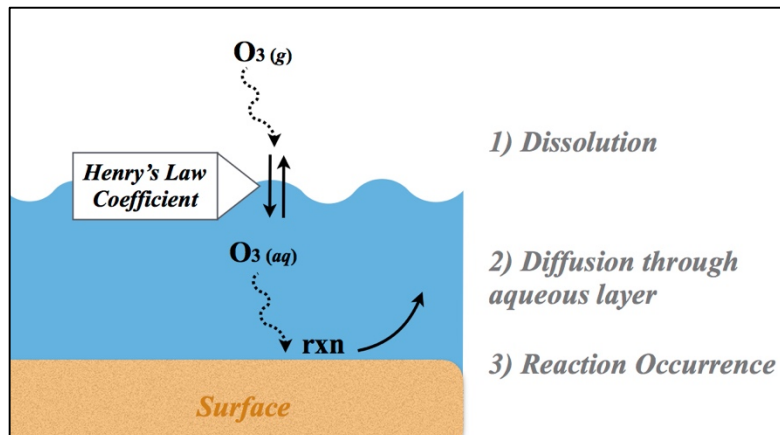


Figure 30. O_3 gas dissolution for solid-aqueous interface reactivity. The process shows the dissolution of O_3 into the aqueous phase, diffusion of solubilized O_3 through the layer, and then eventual reaction on the mineral surface. Diffusion into the aqueous layer is dependent on the Henry's law coefficient for O_3 (Finlayson-Pitts and Pitts, 2000).

Mogili et al. proposed that, given spectroscopic evidence of the formation of water monolayers on $\alpha\text{-Fe}_2\text{O}_3$, it is possible to treat the adsorbed water as a bulk liquid-like environment and therefore O_3 uptake can be more accurately analyzed through a resistance model which accounts for mass accommodation, liquid solubility of O_3 , and aqueous phase reaction. For their experiments, they found that O_3 uptake under high RH was enhanced by O_3 diffusion into the aqueous layer, though their experiments displayed a transitional behavior that implied variable chemistry bridging dry reactivity with liquid-like bulk reactivity. Their findings also corroborate the hypothesis that water surface coverage does not reach uniform layer coatings until high water vapor pressures, at approximately 60% RH.

3.3 Impact of Surface Adsorbed Volatile Organic Compounds (VOCs)

Though accounting for surface reactivity and RH provide us with an understanding of some of the variability within the atmospheric chemistry of aerosol, it is still an oversimplified model of atmospheric conditions. Our main objective for this research is to elucidate variability due to the broader atmospheric complexities such as the processing of mineral dust by VOCs. As previously mentioned, these compounds are primarily found in the atmosphere due to the production of home-cleaning products and cosmetics and released through biogenic production from plants and industrial processes. When mineral dust is transported throughout the atmosphere, it travels over regions with high concentrations of these compounds. In the particular case of Jing-Jin-Ji, mineral dust from the Gobi travels over wide forested areas, interacting with various forms of aerosol. Previous research has highlighted the reactivity of VOCs with mineral dust and as such, it is necessary to understand how this processing of the surface can affect reactivity with O₃ (Romanias et al., 2016).

In this study, kaolinite was reacted with gaseous limonene and α -pinene under various RH values as a model for mineral dust processing throughout atmospheric transport. Upon coating, the mineral surface was exposed to a constant O₃ flow, allowing for the quantification of overall $\gamma_{\text{BET},\text{O}_3}$. Comparison of these calculations with those of the unprocessed mineral dust yielded the results graphed in Figure 31. At 25% RH, the non-coated kaolinite had an $\gamma_{\text{BET},\text{O}_3}$ of $2.95 (\pm 0.49) \times 10^{-9}$, whereas limonene and α -pinene processing increased the uptake to $2.38 (\pm 0.29) \times 10^{-7}$, and $2.51 (\pm 0.23) \times 10^{-7}$, respectively. As can be seen through the data, $\gamma_{\text{BET},\text{O}_3}$ increases by almost 2 orders of

magnitude with the processed dust, indicating further interactions between the adsorbed VOC products and the O_3 .

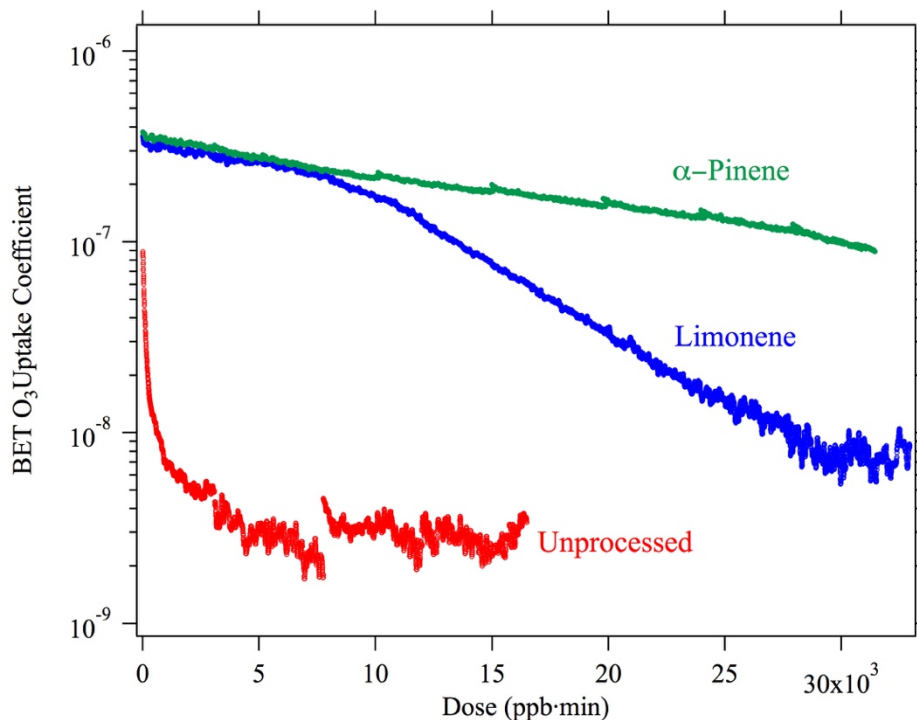


Figure 31. γ_{BET,O_3} for O_3 on unprocessed (red), limonene (blue), and α -pinene (green) kaolinite at 25% RH as a function of dose. VOC-coated kaolinite shows a two order of magnitude increase in reactivity.

Differences in reactivity between the VOC-coated dusts could be due to additional reactivity provided by the functional groups on each compound. Terpene ozonolysis shows the formation of highly reactive Criegee intermediates or zwitterions that can then proceed through a series of unimolecular reactions to form peroxy radicals such as H_2O_2 and SOA (Zhang et al. 2006). Reactivity of various terpenes depends on the substitution and stability of the alkene in question, and thus different compounds, in this

case the adsorbed products of α -pinene and limonene, exhibit distinctive reaction processes.

For instance, upon reaction on the mineral dust, α -pinene forms its main product, α -terpineol, as seen in Figure 32. Following the protonation of the reactive endocyclic alkene by a surface H^+ or Brønsted Acid site, you see a breaking of the bridgehead and a carbocation rearrangement to allow for the nucleophilic attack by water onto the tertiary terminal carbocation.

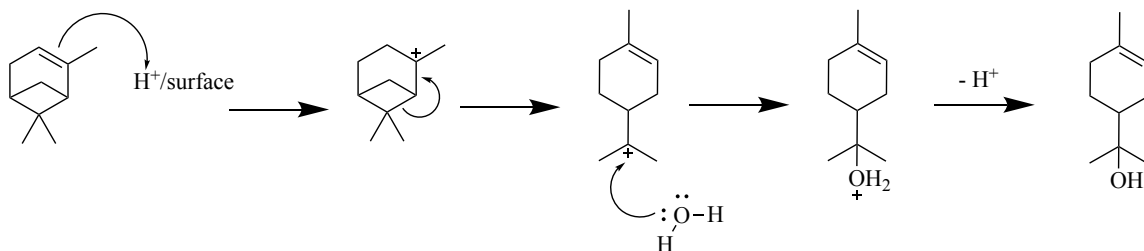


Figure 32. Proposed major reaction scheme for α -pinene on kaolinite forms α -terpineol. Product formation shows the breaking of the bridgehead, a carbocation rearrangement, and a nucleophilic attack to form its main product: α -terpineol. (Edziah et al., 2017)

Studies conducted on the aqueous-phase ozonolysis of α -terpineol show that it is highly reactive with O_3 , as it undergoes the ozonolysis outlined in Figure 33 (Leviss et al., 2016). Through these studies, α -pinene's endocyclic alkene has been shown to be more reactive than a terminal alkene, which could explain the heightened reactivity of the surface-adsorbed α -terpineol product, as it also possesses the reactive endocyclic alkene. Given the added site for O_3 reactive collision, this could explain the larger γ_{BET,O_3} in comparison to limonene, the other VOC evaluated, as seen in Figure 31.

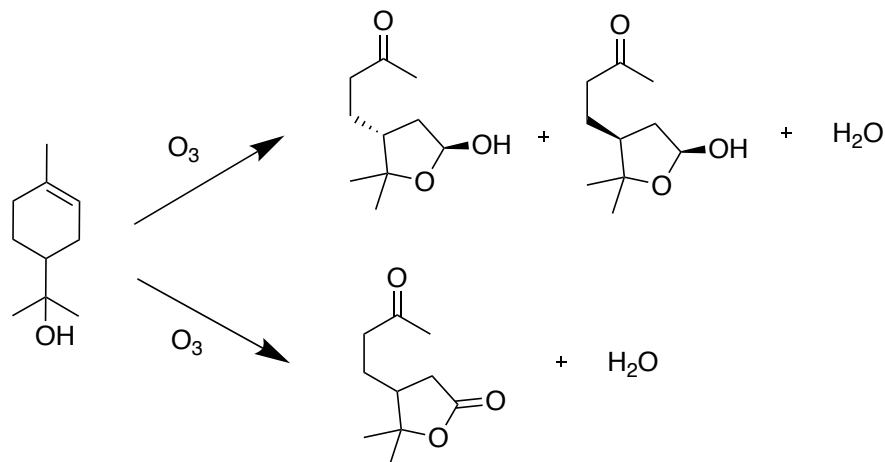


Figure 33. Proposed major reaction schemes for aqueous-phase ozonolysis of α -terpineol show lactol (above) and lactone (below) products. (Leviss, 2016)

It is important to note, however, that gas-phase ozonolysis has been shown to differ from aqueous phase ozonolysis in mechanism and product formation. Gas-phase experiments show the fragmentation of α -terpineol into non-oxidized compounds such as methylglyoxal, ethanedial, 4-methyl-3-cyclohexen-1-one, 6-hydroxy-hept-5-en-2-one, 1,4-butanedial, and 4-oxopentanal, seen in Figure 34 (Forester and Wells, 2009; Wells, 2005). However, these highly oxidized products may be the result of OH radical formation in the system, which push forward the oxidation of the ozonolysis products. In fact, Leviss et al. found that for experiments of α -terpineol on kaolinite, you saw similar product formation to that outlined in Figure 33 for the aqueous phase chemistry (2016). That being said, the formation of water interfaces at the mineral dust surface also allows for the possibility of aqueous phase chemistry such as that predicted by Leviss et al. (2016).

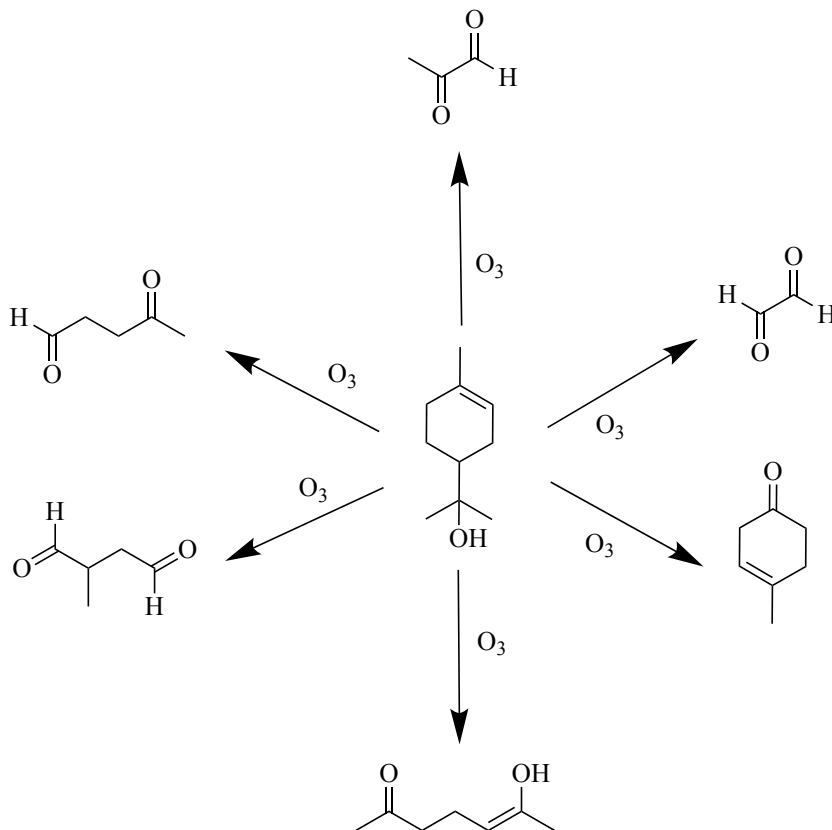


Figure 34. Proposed major reaction products for gas-phase ozonolysis of α -terpineol: methylglyoxal, ethanedial, 4-methyl-3-cyclohexen-1-one, 6-hydroxyhept-5-en-2-one, 1,4-butanedial, and 4-oxopentanal (Forester and Wells, 2009). High degree of oxidation and fragmentation could be due to the secondary oxidation by OH radicals in the system.

Similarly to α -pinene, limonene reacts on kaolinite to form limonene diol and carvone, as seen in Figure 10, repeated below. Both products of this reaction possess terminal alkenes that can also further react through ozonolysis, providing additional sites for O_3 reactivity. Based on the results of Lederer et al., nearly 100% of the adsorbed products are limonene-diol, which would indicate that this is the main adsorbed species available to be oxidized.

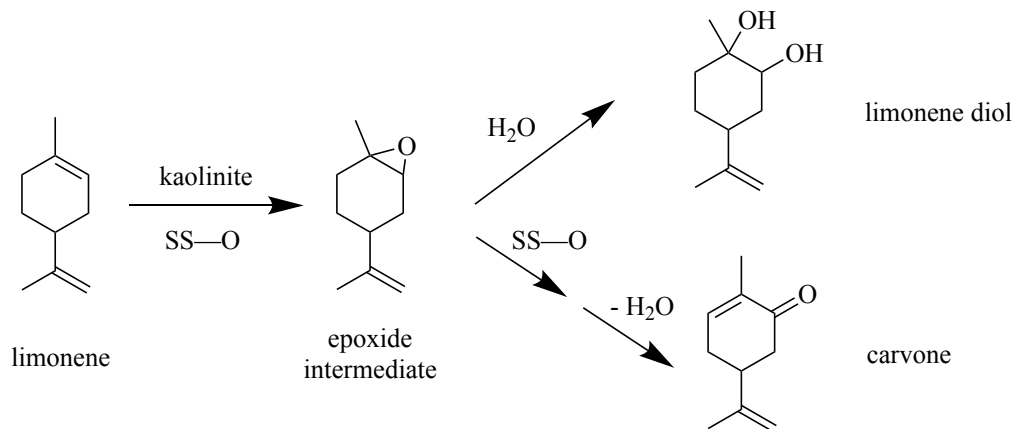


Figure 10. Proposed major reaction scheme for limonene on kaolinite forms limonene diol and carvone. Product formation shows the reaction with a surface oxygen to form an epoxide intermediate which is then broken open to form its main products: limonene diol (above) and carvone (below) (Lederer et al., 2016).

Studies into the ozonolysis of limonene show the formation of 4-Acetyl-1-methylcyclohexene, 2-hydroperoxy-3,4-dimethyl-pent-4-enal, glyoxal, methylglyoxal, oxopentanal, and 3-Isopropenyl-6-oxoheptanal, highlighting similar product formation to the gas-phase ozonolysis of α -terpineol (Forester and Wells, 2009). These predicted products of gas-phase ozonolysis can be seen in Figure 35. However, given that limonene reacts to form its two secondary products on the mineral surface, there is a higher likelihood of finding ozonolysis of limonene diol instead, as proposed in Figure 36. In light of this, α -terpineol is more likely to display heightened reactivity in comparison to its limonene product counterparts, as it possesses an endocyclic alkene with a greater number of substituents, making it more electron-rich and thus better able to attract the electrophilic O₃ (Leviss et al., 2016).

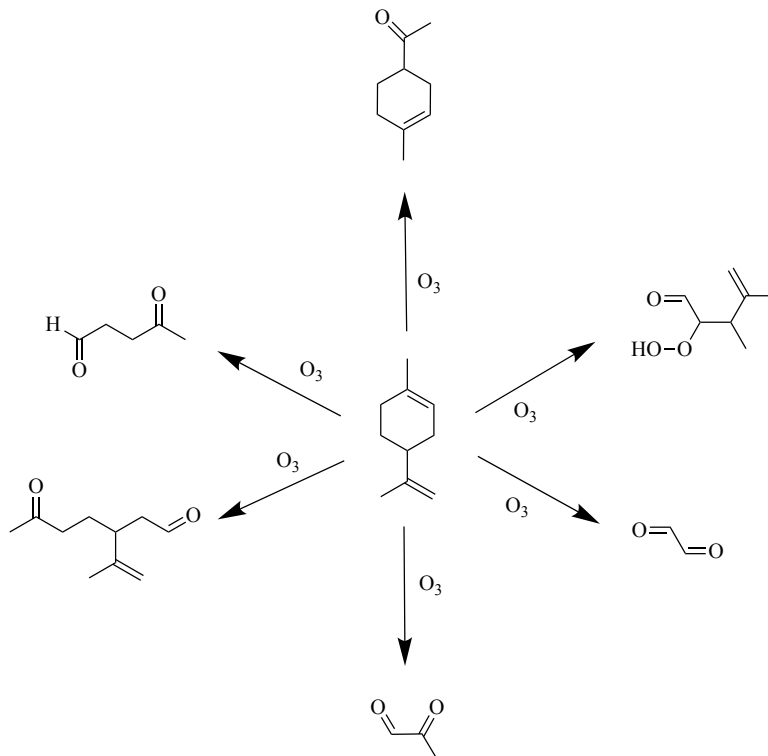


Figure 35. Proposed major reaction products for gas-phase ozonolysis of limonene: 4-Acetyl-1-methylcyclohexene, 2-hydroperoxy-3,4-dimethyl-pent-4-enal, glyoxal, methylglyoxal, oxopentanal, and 3-Isopropenyl-6-oxoheptanal (Forester and Wells, 2009). Shows similar product formation to the gas-phase ozonolysis of α -terpineol. Given that limonene reacts on the kaolinite surface to form limonene diol and carvone, product ozonolysis is more likely to occur on the surface, in lieu of limonene ozonolysis.

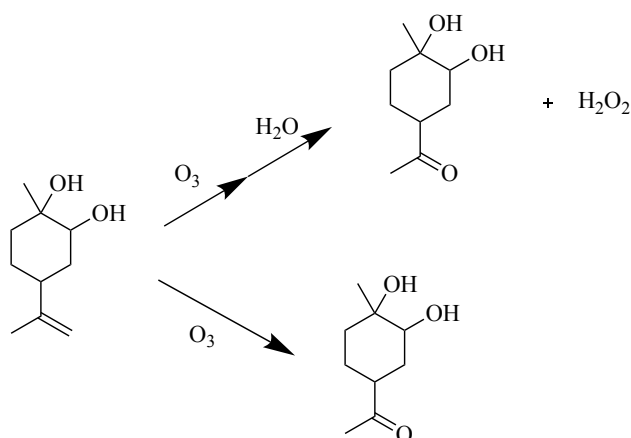


Figure 36. Proposed major reaction scheme for ozonolysis of limonene diol (Coates Fuentes et al., 2017).

In order to determine whether coating products remained adsorbed to the kaolinite surface for continued reactivity, sequential experiments were run to determine relative coating of the mineral surface, as seen in Figure 37. Initially, kaolinite was coated with α -pinene to yield the α -terpineol product and then was reacted with O_3 to generate the ozonolysis products. After running the experiment for approximately 70 ppb-min, the dust was recoated with α -pinene and reacted with O_3 to measure any heightened reactivity from the reintroduction of the more reactive α -terpineol endocyclic alkene. Though there was an initial spike in reactivity, after approximately 5 ppb-min the γ_{BET,O_3} returned to the expected magnitude. This appears to indicate that once ozonolysis of the α -terpineol has occurred, the products remain adsorbed to the surface, blocking available surface sites to which other α -terpineol molecules can adsorb.

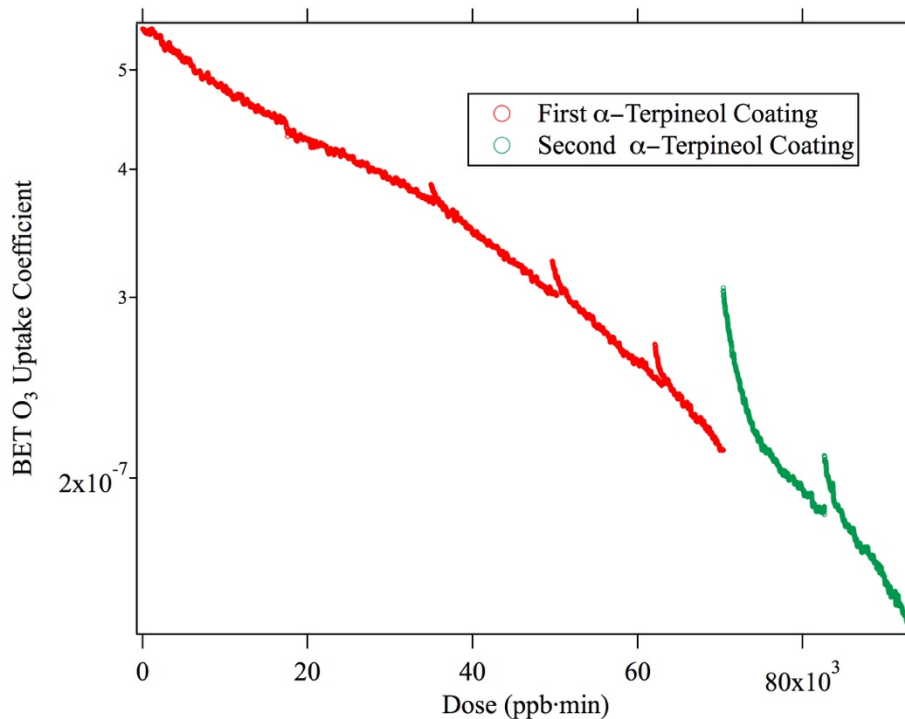


Figure 37. $\gamma_{\text{BET},\text{O}_3}$ for O_3 on α -terpineol-coated dust (red) and α -terpineol coated dust after ozonolysis and re-coating (green) at 25% RH as a function of dose.

Comparison of the two runs shows that the reactivity of the dust is slightly regenerated, as the re-coating introduces additional reactivity, displayed through a slight rise in $\gamma_{\text{BET},\text{O}_3}$. However, full regeneration of the surface sites does not occur, since the $\gamma_{\text{BET},\text{O}_3}$ doesn't approach original values. This indicates that products of ozonolysis remain adsorbed to the surface upon reaction completion.

Having determined this increased reactivity for VOC experiments at 25%RH, we were interested in evaluating similar reactions as a function of RH variability. Figure 38 shows O_3 uptake at various RH values, for both VOC-processed and unprocessed kaolinite. For these experiments, the dust was pre-exposed to VOCs under humidified conditions and then reacted with O_3 . As seen in the figure, O_3 uptake remains significantly higher for processed dusts, even at high RH. This seems to indicate that

even at high RH, where water would have formed a monolayer on the surface, VOCs are still adsorbing to the surface or are potentially interacting in the aqueous phase.

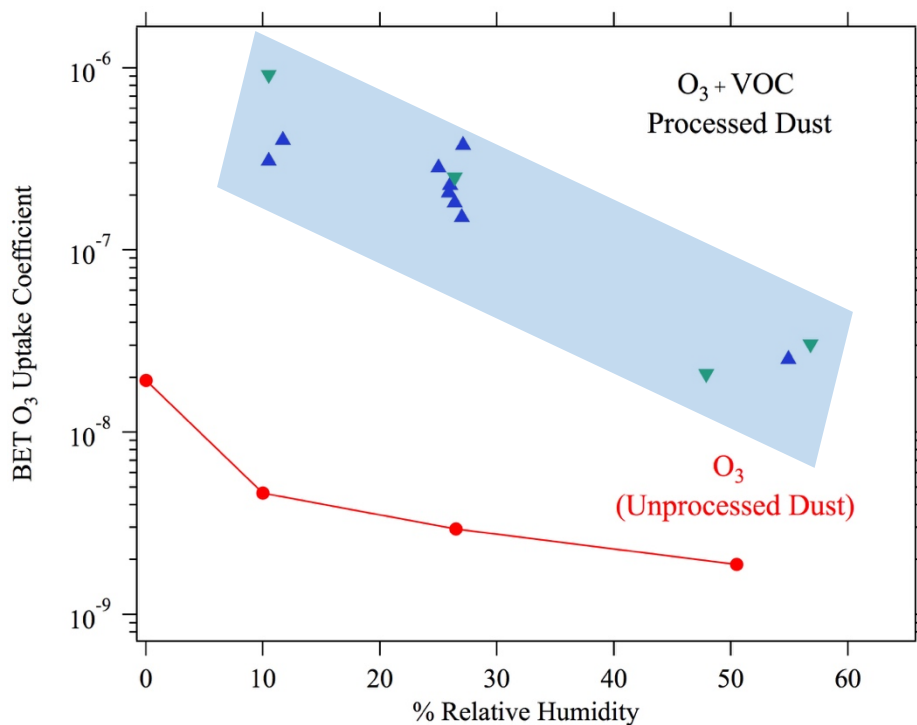


Figure 38. Average $\gamma_{\text{BET},\text{O}_3}$ for O_3 on unprocessed (red), limonene (blue), and α -pinene (green) kaolinite at varying RH values. Figure shows heightened uptake for processed kaolinite at all RH values, indicating sustained reactivity with the secondary products of VOCs with the surface.

3.4 Effect of O_3 Concentration on Rate of Uptake

As with most studies into atmospheric aerosols, one of the variables to be tested is the concentration of the species being analyzed. In particular, atmospheric concentrations of O_3 in rural areas range 30-40 parts per billion (ppb) (Finlayson-Pitts and Pitts, 1997), whereas more populated and industrial areas like Beijing can reach overall concentrations up to approximately 240 ppb (Wei et al., 2015). Given the nature of our laminar flow setup and O_3 generator, the lowest stable concentrations obtained

were around 60 ppb. For this reason, experiments were run on limonene-coated kaolinite with O_3 at concentrations of 60, 132, 207, 370, and 683 ppb, the results of which are displayed on Figure 39. After correcting for O_3 concentration, it was possible to see that at lower concentrations, the surface showed heightened reactivity, with larger γ_{BET,O_3} for a prolonged time. This indicates that the γ_{BET,O_3} on kaolinite displays a dependence on O_3 concentration. Therefore, our model system, when applied to atmospherically relevant concentrations of O_3 , shows increased reactivity in comparison to literature studies showing lower uptake coefficients.

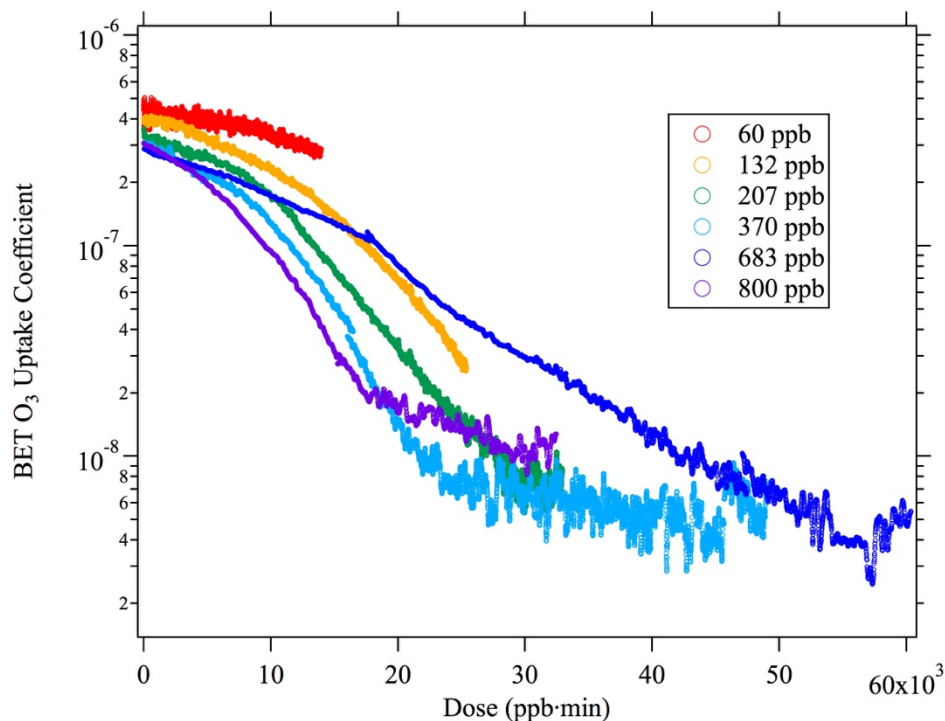


Figure 39. γ_{BET,O_3} for O_3 on limonene-coated Kaolinite at 25% RH as a function of dose, at concentrations of 60, 132, 207, 370, 683, and 800 ppb. Figure shows greater sustained probability of a reaction at lower atmospheric concentrations of O_3 .

These results can be more clearly seen in Figure 40, where $\gamma_{\text{BET},\text{O}_3}$ values were significantly higher for lower concentrations of O_3 at all dose points, with the 60 ppb's lowest $\gamma_{\text{BET},\text{O}_3}$, at 10000 ppb-min being higher than the 800 ppb's highest $\gamma_{\text{BET},\text{O}_3}$, at 0 ppb-min. This indicates that most literature studies, which have been run at ppm concentrations, are largely underestimating O_3 reactivity.

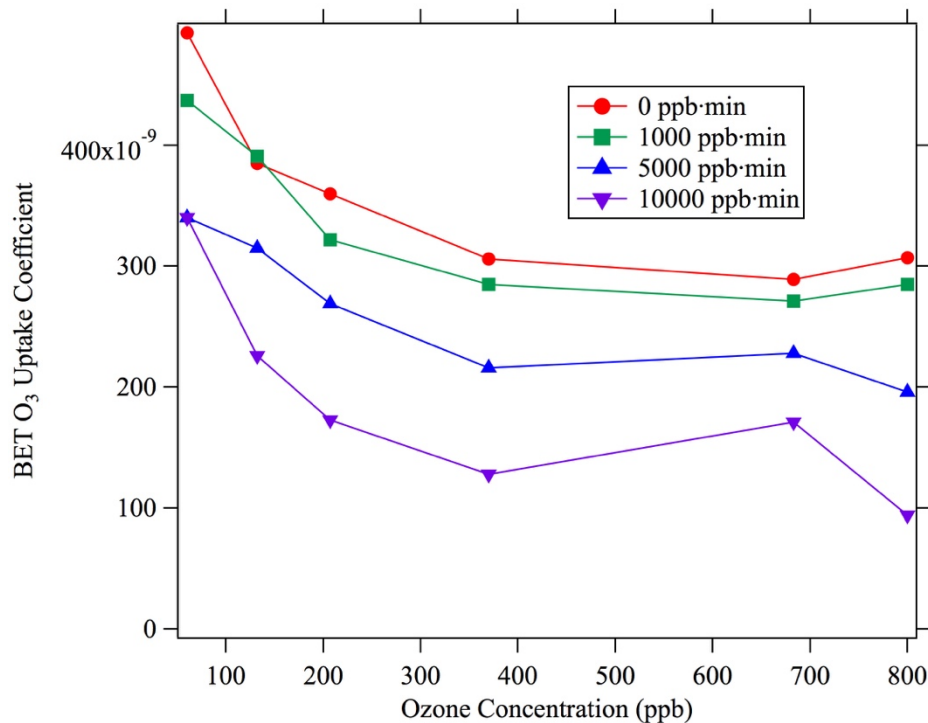


Figure 40. $\gamma_{\text{BET},\text{O}_3}$ for O_3 on kaolinite at 0, 1000, 5000, and 10000 ppb-min as a function of O_3 concentration.

These observations coincide with literature results such as those presented by Roscoe and Abbatt, who concluded that under 0% RH, Al_2O_3 reactivity dependence on O_3 concentration was only noticeable at lower concentrations, which they attribute to the saturation of the alumina surface with O_3 , followed by oxide production under pseudo-first order kinetics (2005).

3.5 Impact of SO₂ on O₃ Reactivity

In addition to interacting with VOCs, mineral dusts have been shown to interact with various atmospheric pollutants such as SO₂. Literature studies into the reactivity of SO₂ in the atmosphere have developed a proposed mechanism for the formation of SO₃²⁻ from SO₂ by reactive surface hydroxyl groups and O₃ adsorbed to the mineral surface (Li et al., 2007). This mechanism is outlined in reaction schemes 15-17. Following the initial adsorption of SO₂ onto the surface, the molecule can form adsorbed SO₃²⁻ on the surface, which is then readily oxidized to SO₄²⁻ by oxidants in the system, in certain cases adsorbed O₃ on the surface (Li et al., 2007).

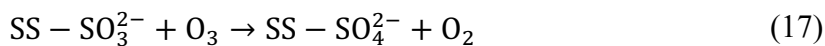
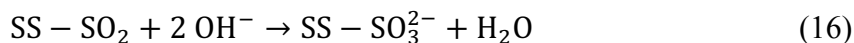


Figure 41 shows $\gamma_{\text{BET},\text{O}_3}$ for simultaneous SO₂ and O₃ exposure to the surface on both processed and unprocessed dusts. For these experiments, RH was maintained at approximately 25%RH and VOC processing was modeled by pre-exposure to α -pinene. When comparing $\gamma_{\text{BET},\text{O}_3}$ as a function of exposure to SO₂ and α -pinene, used in these experiments as a model for VOC processing, we see that SO₂ exposure appears to increase O₃ reactivity by two orders of magnitude, from $2.95 (\pm 0.49) \times 10^{-9}$ on unprocessed kaolinite to $1.32 (\pm 0.08) \times 10^{-7}$. Following similar increases, $\gamma_{\text{BET},\text{O}_3}$ values for pinene experiments show elevated reactivity under VOC processing. However, when

exposed to α -pinene-processed kaolinite, $\gamma_{\text{BET},\text{O}_3}$ remains approximately the same regardless of the presence of SO_2 , with a percent difference of approximately 10.4%.

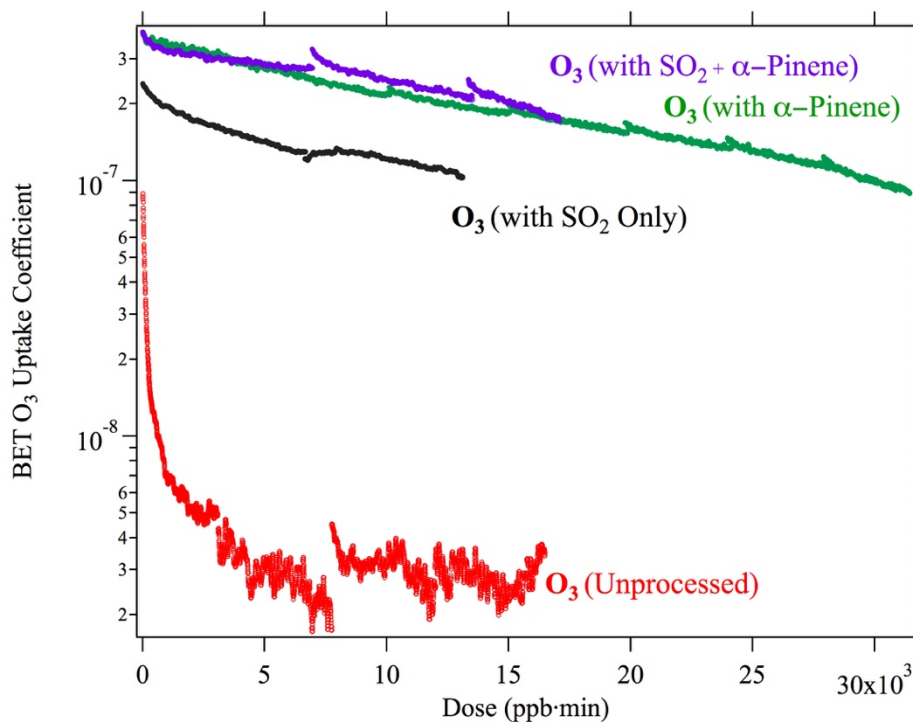


Figure 41. $\gamma_{\text{BET},\text{O}_3}$ for kaolinite with simultaneous SO_2 (black), α -pinene processing (green), and α -pinene processing with simultaneous SO_2 (purple), compared to unprocessed kaolinite (red) at 25% RH as a function of dose. Figure shows heightened reactivity for processed dusts. However, for the experiments involving α -pinene, α -pinene appears to dominate reactivity when compared to SO_2 exposure.

The average $\gamma_{\text{BET},\text{O}_3}$ values obtained from Figure 41 are summarized in Table 2 and Figure 42. Figure 42 shows incremental reactivity as a function of greater processing.

Table 2: BET uptake coefficients for O₃ at 25% RH as a function of α -pinene and SO₂ exposure

		SO ₂	
		Yes	No
α -Pinene	Yes	$2.77 (\pm 0.15) \times 10^{-7}$	$2.51 (\pm 0.23) \times 10^{-7}$
	No	$1.32 (\pm 0.08) \times 10^{-7}$	$2.95 (\pm 0.49) \times 10^{-9}$

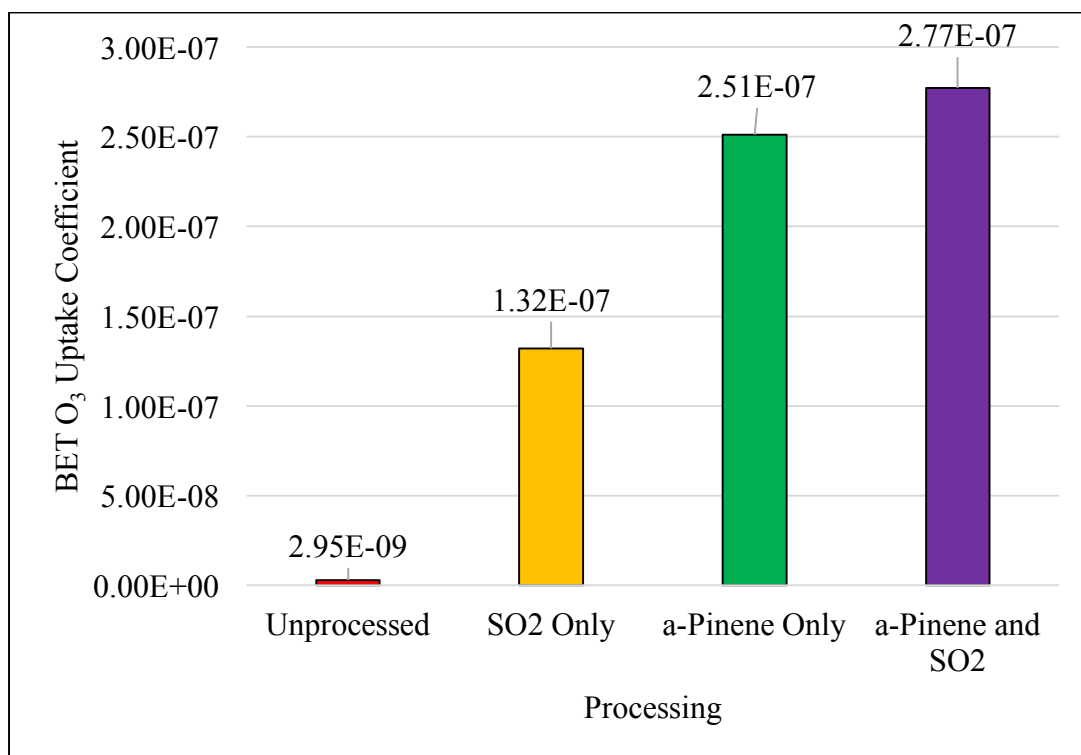


Figure 42. Average $\gamma_{\text{BET},\text{O}_3}$ for kaolinite with simultaneous SO₂ (black), α -pinene processing (green), and α -pinene processing with simultaneous SO₂ (purple), compared to unprocessed kaolinite (red) at 25% RH as a function of dose. Figure shows heightened reactivity for processed dusts. However, the difference between the α -pinene only and the α -pinene with simultaneous SO₂ is minimal, indicating that α -pinene dominates the reactivity.

In light of SO₂'s apparent low impact on $\gamma_{\text{BET},\text{O}_3}$ for α -pinene processed dusts, O₃ reactivity with α -pinene seems to dominate in the reaction scheme, with SO₂ having a negligible effect on the overall uptake. This raises the question, does SO₂ reactivity decrease with α -pinene coatings since O₃ reactivity is controlled by the organic? To determine this, we measured SO₂ uptake ($\gamma_{\text{BET},\text{SO}_2}$) in order to visualize whether there was a decrease in reactivity for SO₂.

Figure 43 shows uptakes for both O₃ and SO₂ during α -pinene experiments. The unprocessed experiments show similar $\gamma_{\text{BET},\text{O}_3}$ and $\gamma_{\text{BET},\text{SO}_2}$ values. For these experiments, O₃ and SO₂ appear to be depleting at similar rates, indicating possible reactivity dependence on each other. However, the value for $\gamma_{\text{BET},\text{SO}_2}$ is slightly higher than that for $\gamma_{\text{BET},\text{O}_3}$, which would seem to indicate preferential reactivity for the SO₂ with the unprocessed mineral surface. For the α -pinene processed experiments, however, $\gamma_{\text{BET},\text{O}_3}$ is significantly higher and more sloped than $\gamma_{\text{BET},\text{SO}_2}$, as it is primarily interacting with α -pinene. Despite this higher O₃ reactivity, $\gamma_{\text{BET},\text{SO}_2}$ remains approximately the same. This would seem to indicate that SO₂ is still reacting with the mineral surface or potentially reacting with the VOC ozonolysis products to form organosulfates on the surface. Further experiments are required to determine the products of these reactions.

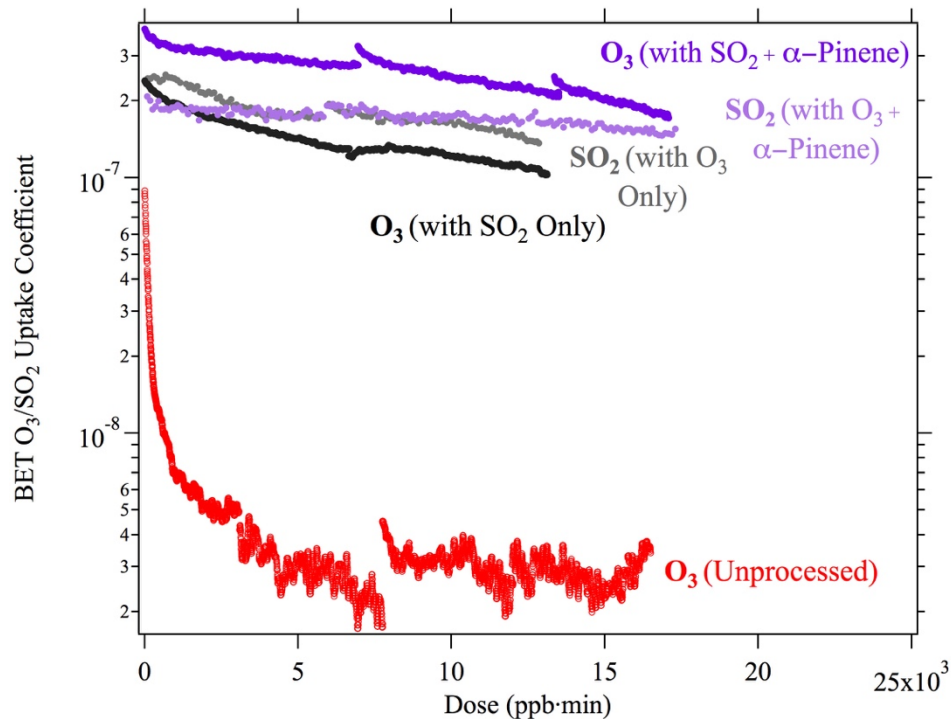


Figure 43. $\gamma_{\text{BET},\text{SO}_2}$ (grey) and $\gamma_{\text{BET},\text{O}_3}$ (black) for the simultaneous exposure of O_3 and SO_2 on unprocessed kaolinite and $\gamma_{\text{BET},\text{SO}_2}$ (purple) and $\gamma_{\text{BET},\text{O}_3}$ (light purple) on α -pinene-coated kaolinite at 25% RH as a function of dose compared to unprocessed dust (red). Figure shows that unprocessed mineral dust has greater $\gamma_{\text{BET},\text{SO}_2}$ than $\gamma_{\text{BET},\text{O}_3}$. However, when the dust has been processed by α -pinene, O_3 reactivity is dominated by the α -pinene product alkenes, which translates to higher $\gamma_{\text{BET},\text{O}_3}$

Having determined these trends in O_3 reactivity as a function of VOC and SO_2 exposure, it is important to examine the other side of the reaction to understand what is occurring with the SO_2 on the surface. In order to do this, $\gamma_{\text{BET},\text{SO}_2}$ was calculated for the simultaneous O_3/SO_2 experiments. Comparison of the data for trends in variability could clarify a possible pathway for SO_2 oxidation on mineral surfaces.

Comparison of $\gamma_{\text{BET},\text{SO}_2}$ as a function of exposure to O_3 and α -pinene yielded the trends outlined in Table 3. $\gamma_{\text{BET},\text{SO}_2}$ appears to increase slightly with exposure to both O_3

and VOC, with α -pinene having a negligible effect over $\gamma_{\text{BET},\text{SO}_2}$, as the values for processed and unprocessed dust are $1.78 (\pm 0.07) \times 10^{-7}$ and $1.73 (\pm 0.07) \times 10^{-7}$. Despite this slight variability, the overall differences in $\gamma_{\text{BET},\text{SO}_2}$ throughout the experiments are small, and within the error for the setup. It is possible that this regularity in the $\gamma_{\text{BET},\text{SO}_2}$ values is due to the fact that SO_2 readily converts into SO_3^{2-} on the kaolinite surface, following reactions 15 and 16. Therefore, the $\gamma_{\text{BET},\text{SO}_2}$ that we are measuring is to be attributed to this conversion, which is able to occur regardless of O_3 's presence in the system (Li et al., 2007).

Table 3: BET Uptake Coefficients for SO_2 at 25%RH as a function of α -pinene and O_3 exposure

		O_3	
		Yes	No
Pinene	Yes	$1.78 (\pm 0.07) \times 10^{-7}$	
	No	$1.73 (\pm 0.07) \times 10^{-7}$	$1.36 (\pm 0.17) \times 10^{-7}$

Since these trends in reactivity for SO_2 show a very limited change in reaction probability as a function of mineral dust processing, it may be necessary to develop further experiments to test the reactivity of SO_2 on the mineral surface. Among them could be the evaluation of adsorbed SO_3^{2-} and SO_4^{2-} formation on the mineral surface through DRIFTS-FTIR experiments following a similar procedure to Li et al. (2007).

Chapter 4: Conclusion

4.1 Summary of Main Results

Experiments into the reactivity of O₃ on the mineral surface showed that O₃ readily reacts with sites on the mineral surface, as reported in various literature studies. The evaluation of the RH-dependence of O₃ uptake showed that higher RH values exhibited lower reactivity consistent with saturation of the surface reactive sites by water. This hints at the possibility of competitive inhibition of the available surface sites, wherein water molecules are adsorbing to the Lewis Acid sites that would react with O₃ and are limiting reactivity. However, the sustained uptake on the surface indicates possible diffusion of the O₃ into the aqueous interface, allowing for aqueous-phase reactivity to occur. Additionally, the water coating on the surface may be adsorbing in micro-puddles rather than even microfilms and therefore there are remaining “dry” sites along the surface that O₃ can adsorb to.

Atmospheric processing of the dust by terpene VOCs, in this case limonene and α -pinene, shows heightened reactivity with O₃ by two orders of magnitude. The increased reactivity is likely due to the presence of highly reactive alkenes in the adsorbed products of the terpene oxidation on the mineral dust surface. In the case of α -pinene, the main product, α -terpineol, possesses an endocyclic alkene that readily reacts with O₃ to form SOA. On the other hand, limonene reacts with the mineral surface to form limonene diol, which possesses a terminal alkene that will also react with O₃, though less favorably than α -terpineol's, yielding a lower $\gamma_{\text{BET},\text{O}_3}$. Thus, the presence of

these SOA on the mineral surface provides additional sites for O₃ reactivity, serving as a sink for greater concentrations of tropospheric O₃.

Atmospheric processing by SO₂ also shows an increase in $\gamma_{\text{BET},\text{O}_3}$ by two orders of magnitude. When comparing between simultaneous SO₂ and α -pinene reactivity, α -pinene appeared to dominate reactivity. However, evaluation of the SO₂ concentrations throughout the experiment showed that they were largely unchanged between VOC-coated and uncoated experiments. This seems to indicate that SO₂ is still reacting with the mineral surface or could be reacting with the products of the VOC ozonolysis to form organosulfates on the surface.

When analyzing the concentration-dependence of $\gamma_{\text{BET},\text{O}_3}$, results showed that reactivity was higher at lower atmospheric concentrations of O₃. In essence, under atmospherically relevant concentrations of O₃, below 100 ppb, the mineral surface is able to react for significantly longer before reaching steady state, providing a greater sink for tropospheric O₃.

As a whole, these experiments highlight a large dependence of $\gamma_{\text{BET},\text{O}_3}$ on atmospheric processing by RH, VOC's, and SO₂, as seen in Figure 44. As such, current computational models for atmospheric concentrations of trace gases which do not take into account various forms of mineral dust processing are underestimating the reactivity of trace gases on the mineral surface. As such, they should be improved to account for additional sources of reactivity in order to provide more accurate predictions of criteria air pollutant concentrations.

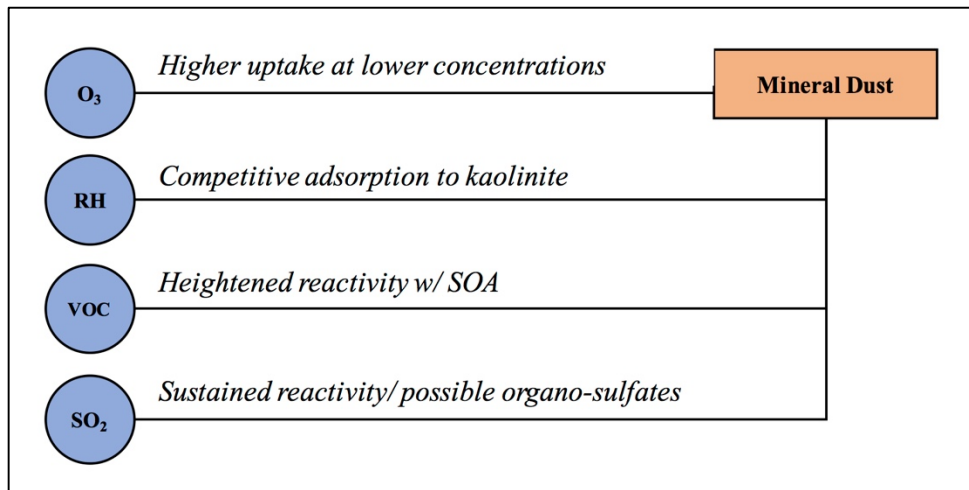


Figure 44. Effects of various forms of processing on $\gamma_{\text{BET},\text{O}_3}$ on kaolinite.

These results help clarify the aerosol chemistry for regions such as Jing-Jin-Ji, with large atmospheric concentrations of atmospheric NO_2 , SO_2 , and O_3 , as well as proximity to the Gobi Desert, a source of mineral aerosol. Furthermore, extrapolation of air quality measures from these data may allow policy-makers to make more educated policy decisions in the future based on the restriction of processes that emit large amounts of criteria air pollutants. For Jing-Jin-Ji in particular this may mean the reduction of coal burning, as well as restrictions in fuel consumption.

4.2 Areas for Future Work

Future studies into the reactivity of trace gasses on mineral aerosol should include a comprehensive evaluation of various forms of atmospheric processing, most importantly VOC-coating. As we see throughout our experiments, organic coatings on the mineral surface provide further sites for reactions to occur, leading to an increase in reaction probability. In light of this, experimental analyses of mineral aerosol should

address the multiple types of hydrocarbons present, both biogenic and anthropogenic, within a given region. Among these could be the products of biomass burning, such as catechol, which have been shown to adsorb to the mineral surface following a binuclear bidentate binding as seen in Figure 45:

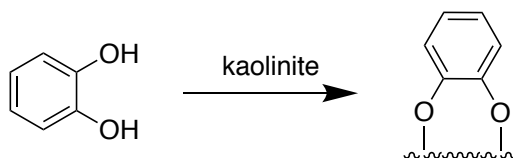


Figure 45. Catechol adsorption onto mineral dust surface through a binuclear bidentate catecholate. (Woodill et al., 2013)

Former studies have characterized the aqueous-phase ozonolysis of catechol to form *cis,cis*-muconic acid and oxalic acid, as seen in Figure 46. However, little is known about the ozonolysis of surface-bound catechol.

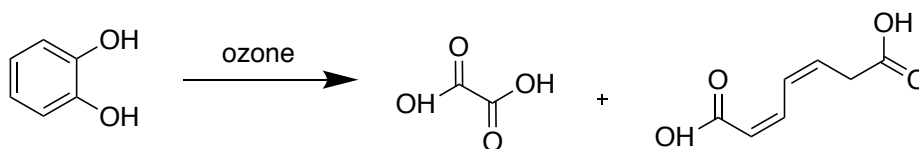


Figure 46. Ozonolysis of catechol to form oxalic acid (left) and *cis,cis*-muconic acid (right). (Woodill et al., 2013)

Incorporation of other VOCs will help provide a better understanding of the chemistry of different regions' atmospheric species, with the possibility of developing more accurate parameters for prediction models.

For our setup in particular, the measurement of SO_2 oxidation on the surface was uncertain, as flaws in the setup and data collection intervals could have been altering our results. We hypothesized that one possibility for our limited variability in $\gamma_{\text{BET},\text{SO}_2}$ was that SO_2 was readily converting into SO_3^{2-} , which could happen on the mineral surface

without O₃ oxidation. In order to evaluate this possibility, DRIFTS-FTIR experiments could be run to determine SO₃²⁻ and SO₄²⁻ formation as a function of time, in a manner similar to Li et al. (2007). Monitoring of the formation of adsorbed species by integrating their characteristic SO₃²⁻ and SO₄²⁻ vibrational modes could be an indication of SO₄²⁻ formation on the dust surface, which would confirm our hypothesis for heterogeneous reactivity on mineral aerosol. Another alternative for reactivity could be the formation of organosulfates on the dust surface. DRIFTS-FTIR and GC/MS analyses of the adsorbed species could also provide evidence for this secondary reactivity of the VOC ozonolysis products with the SO₂.

As seen in Figure 47, further research for Jing-Jin-Ji should be conducted on the other major chemical compound mass percent contributors such as NO₃⁻ and NH₄⁺ (Shen et al., 2018). The prevalence of ammonium salts within PM_{2.5} may be evaluated for possible sources of reactivity. As a main product of processed gaseous NH₃, a trace gas associated with agriculture, as well as a main emission from oceans, microbial activity, soils, and wildlife, NH₄⁺ may be influencing the reactivity of various aerosol throughout the atmosphere (Ianniello et al., 2011). Additionally, through the gas-phase oxidation of NO₂, mainly associated with fuel burning, we see the formation of NO₃⁻, which, unlike the other mass contributors, has limited seasonal variability. Given the role of traffic emissions on the prevalence of these species, a better understanding of their chemistry could lead to improved regional regulations on motor fuel and vehicular restrictions.

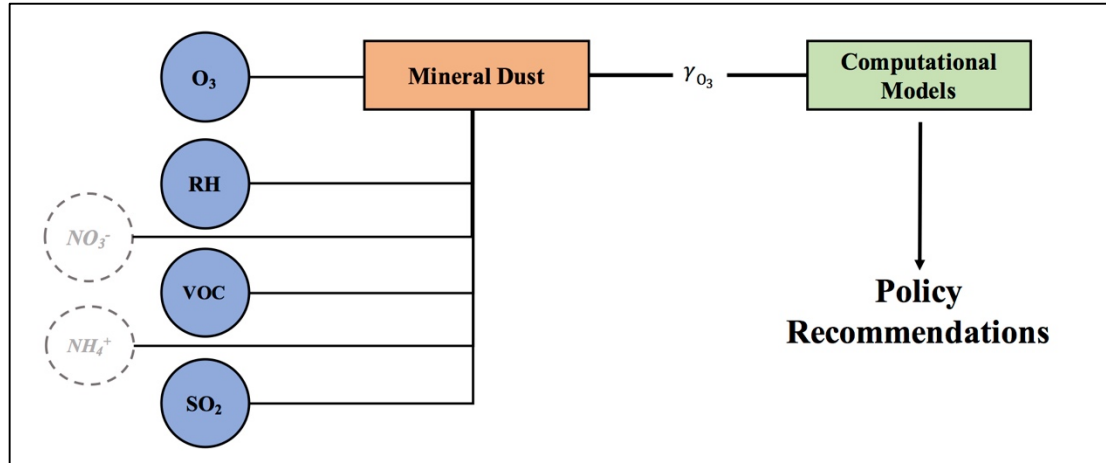


Figure 47. Adjusted conceptualization of research variables as knobs that can be turned on or off in order to introduce further complexity to the experiments. Incorporation of NO_3^- and NH_4^+ , the two other major mass contributors into Jing-Jin-Ji's pollution, into the experimental procedure could provide a more complete understanding of the chemistry in the region.

Work Cited:

- Buseck, P. R.; Posfai, M. Airborne minerals and related aerosol particles: Effects on climate and the environment. *Proc. Natl. Acad. Sci.* **1999**, *96*, 3372-3379.
- Coates Fuentes, Z. L.; Kucinski, T. M.; Hinrichs, R. Z. Ozone Decomposition on Kaolinite as a Function of Monoterpene Exposure and Relative Humidity. *ACS Earth and Space Chem.* **2018**, *2*, 21-30.
- Cwiertny, D. M.; Young, M.A.; Grassian, V. H.. Chemistry and Photochemistry of Mineral Dust Aerosol. *Annu. Rev. Phys. Chem.* **2008**, *59*, 27-51.
- Edziah, J.J. Senior Honors Thesis. **2017**.
- EPA. National Ambient Air Quality Standards Table. **2016**.
- Ewing, G.E. Ambient thin film water on insulator surfaces. *Chem. Rev.* **2006**, *106*, 1511-1526
- Finlayson-Pitts, B.J.; Pitts, J.N. Tropospheric Air Pollution: Ozone, Airborne Toxics, Polycyclic Aromatic Hydrocarbons, and Particles. *Science.* **1997**, *276*, 1045-1052.
- Finlayson-Pitts, B.J.; Pitts, J.N. Upper and Lower Atmosphere. **2000**, 298-325.
- Forester, C. D.; Wells, J. R. Yields of carbonyl products from gas-phase reactions of fragrance compounds with OH radical and ozone. *Environ. Sci. Technol.* **2009**, *43*, 3561-3568.
- Grosjean, D.; Williams, E.L.; Grosjean, E.; Andino, J.M.; Seinfeld, J.H. Atmospheric Oxidation of Biogenic Hydrocarbons: Reaction of Ozone with β -pinene, D-Limonene and *trans*-Caryophyllene. *Environ. Sci. Technol.* **1993**, *27*, 2754-2758.
- Ianniello, A.; Spataro, F.; Esposito, G.; Allegrini, I.; Hu, M.; Zhu, T. Chemical characteristics of inorganic ammonium salts in PM_{2.5} in the atmosphere of Beijing (China). *Atmos. Chem. Phys.* **2011**, *11*, 10803-10822.
- IPCC. Climate Change 2001: The Scientific Basis. Contribution of Working group I to the Third Assessment Report of the Intergovernmental Panel on Climate Change. *Cambridge University Press*: Cambridge, U.K. **2001**.
- Jia, H.; Wang, L. Peering into China's thick smog. *C. & En.* **2017**, 19-22.
- Karagulian, F.; Rossi, M.J. The Heterogeneous Decomposition of Ozone on Atmospheric Mineral Dust Surrogates at Ambient Temperature. *Wiley Interscience.* **2005**. [Online]

- Knopf, D.A; Pöschl, U.; Shiraiwa, M. Radial Diffusion and Penetration of Gas Molecules and Aerosol Particles through Laminar Flow Reactors , Denuders, and Sampling Tubes. *Anal. Chem.* **2015**, *87*, 3746-3754.
- Lederer, M.R.; Staniec, A. R.; Coates Fuentes, Z. L, Van Ry, D.A; Hinrichs, R.Z. Heterogenous Reactions of Limonene on Mineral Dust: Impacts of Adsorbed Water and Nitric Acid. *J. Phys. Chem. A* **2016**, *120*, 9545-9556.
- Leviss, D.H.; Van Ry, D.A; Hinrichs, R.Z. Multiphase Ozonolysis of Aqueous α -Terpineol. *Environ. Sci. Technol.* **2016**, *50*, 11698-11705.
- Levy, H II. Normal atmosphere: large radical and formaldehyde concentrations predicted. *Science.* **1971**, *173*,141-143.
- Lelieveld, J.; Dentener, F. J. What controls tropospheric ozone? *J. Geophys. Res.* **2000**, *105*, 3531-3551.
- Li, L.; Chen, Z. M.; Zhang, Y. H., Zhu, T.; Li, S.; Li, H. J.; Zhu, L. H.; Xu, B. Y. Heterogenous oxidation of sulfur dioxide by ozone on the surface of sodium chloride and its mixtures with other components. *J. Geophys. Res.* **2007**, *112*, 1-13.
- Mogili, P. K.; Kleiber, P. D.; Young, M. A.; Grassian, V. H. Heterogenous Uptake of Ozone on Reactive Components of Mineral Dust Aerosol: An Environmental Aerosol Reaction Chamber Study. *J. Phys. Chem.* **2006**, *110*, 13799-13807.
- Ma, Q.; Liu, Y.; He, H. The Utilization of Physisorption Analyzer for Study ing the Hygroscopic Properties of Atmospherically Relevant Particles. *J. Phys. Chem.* **2010**, *114*, 4232-4237.
- Roscoe, J.; Abbatt, J. P. D. Diffuse Reflectance FTIR Study of the Interaction of Alumina Surfaces with Ozone and Water Vapor. *J. Phys. Chem.* **2005**, *109*, 9028-9034.
- Romanias, M. N.; Ourrad, H.; Thevenet, F.; Riffault, V. Investigating the Heterogeneous Interaction of VOCs with Natural Atmospheric Particles: Adsorption of Limonene and Toluene on Saharan Mineral Dusts. *J. Phys. Chem A.* **2016**, *120*, 1197-1212.
- Shaked, Y.; Lis, H. Disassembling iron availability to phytoplankton. *Frontiers in Microbiology.* **2012**, *3*, 1-26.
- Shen, R.; Schafer, K.; Schnelle-Kreis, J.; Shao, L.; Norra, S.; Kramar, U.; Michalke, B.; Abbaszade, G.; Streibel, T.; Zimmermann, R.; Emeis, S. Seasonal variability and source distribution of haze particles from a continuous one-year study in Beijing. *Atmospheric Pollution Research.* **2018**, 1-7. <https://doi.org/10.1016/j.apr.2017.12.013>

- Soler, R.; Nicolas, J.F.; Caballero, S.; Yubero, E.; Crespo, J. Depletion of tropospheric ozone associated with mineral dust outbreaks. *Environ. Sci. Pollut. Res.* **2016**, *23*, 19376-19386.
- Tang, M.; Cziczo, D. J.; Grassian, V. H. Interactions of Water with Mineral Dust Aerosol: Water Adsorption, Hygroscopicity, Cloud Condensation, and Ice Nucleation. *Chem. Rev.* **2016**, *116*, 4205–4259.
- Usher, C. R.; Michel, A.E; Grassian, V.H. Reactions on Mineral Dust. *Chem Rev.* **2003**, 4883-4939.
- Wang, K.; Zhang, Y.; Fountoukis, C. Implementation of dust emission and chemistry into the Community Multiscale Air Quality modeling system and initial application to Asian dust storm episode. *Atmos. Chem. Phys.* **2012**, *12*, 10209-10237.
- Wei, W.; Lv, Z.; Wang, L.; Ji, D.; Zhou, Y.; Wang, L. Characterizing ozone pollution in a petrochemical industrial area in Beijing, China: a case study using a chemical reaction model. *Environ. Monit. Assess.* **2015**, 186.
- Wells, J. R. Gas-phase chemistry of α -terpineol with ozone and OH radical: Rate constants and products. *Environ. Sci. Technol.* **2005**, *39*, 6937–6943.
- Woodill, L.A.; O'Neill, E. M.; Hinrichs, R.Z. Impacts of Surface Adsorbed Catechol on Tropospheric Aerosol Surrogates: Heterogeneous Ozonolysis and Its Effects on Water Uptake. *J. Phys. Chem. A* **2013**, *117*, 5620-5631.
- Woodward, S.; Roberts, D. L.; Betts, R. A. A simulation of the effect of climate change-induced desertification on mineral dust aerosol. *Geophys. Res. Lett.* **2005**, 32. [Online]
- World Health Organization. WHO Air quality guidelines for particulate matter, ozone, nitrogen dioxide and sulfur dioxide. **2005**, 1-21.
- Yesilbas, M.; Boily, J. Particle Size Controls on Water Adsorption and Condensation. *Scientific Reports.* **2016**, *6*, 32136.
- Yin, H.; Xu, L. Comparative study of PM₁₀/PM_{2.5}-bound PAHs in downtown Beijing, China: Concentrations, sources, and health risks. Particle Size Controls on Water Adsorption and Condensation. *J. Clean Prod.* **2018**, *177*, 674-683.
- Yu, Z.; Jang, M.; Park, J. Modeling atmospheric mineral aerosol chemistry to predict heterogeneous photooxidation of SO₂. *Atmos. Chem. Phys.* **2017**, *17*, 10001-10017.